

Spectral Signatures of Positive and Negative Polarons in Lead-Halide Perovskite Nanocrystals

Aaron Forde,[†] Talgat Inerbaev,^{‡,§,||} and Dmitri Kilin^{*,†,ID}

[†]Department of Materials Science and Nanotechnology, North Dakota State University, Fargo, North Dakota 58102, United States

[‡]Sobolev Institute of Geology and Mineralogy SB RAS, Novosibirsk 630090, Russia

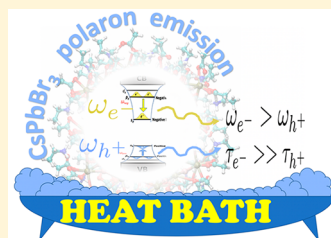
[§]L. N. Gumilyov Eurasian National University, Nursultan 010000, Kazakhstan

^{||}National University of Science and Technology MISIS, 4 Leninskiy pr., Moscow 119049, Russian Federation

^{*}Department of Chemistry and Biochemistry, North Dakota State University, Fargo, North Dakota 58102, United States

Supporting Information

ABSTRACT: APbX_3 ($\text{A} = \text{Cs}$, methylammonium {MA}; $\text{X} = \text{I}$, Br , Cl) lead halide perovskites are of interest for light-emitting applications due to the tunability of their bandgap across the visible and near-infrared spectrum (IR) coupled with efficient photoluminescence quantum yields (PLQYs). It is widely speculated that photoexcited electrons and holes spatially separate into large (Frölich) negative and positive polarons which are stabilized by the A cations. Polarons are expected to be optically active, with recent IR transient absorption experiments showing spectral features consistent with photoionization of the polaron into the continuum band states. For large polarons in the intermediate coupling regime, it would also be expected to observe spectral signatures of transitions within the polaronic potential well producing polaron excited-states. From the polaron excited-state we predict that large polarons should be capable of spontaneous emission (photoluminescence) in the mid-IR to far-IR regime based on the concept of inverse occupations within the polaron potential well. To test this hypothesis, we use density-functional theory (DFT) based calculations using a CsPbBr_3 nanocrystal atomistic model as a host material for either negative (electron) or positive (hole) polarons. We dynamically couple electronic and nuclear degrees of freedom by computing nonadiabatic couplings which allow us to explore nonradiative relaxation of excited polaronic states. Radiative relaxation of excited polaronic states is found from Einstein coefficients for spontaneous emission. Efficiency of polaron emission is determined from rates of nonradiative recombination (k_{NR}) and radiative recombination (k_{R}) as $k_{\text{R}}/(k_{\text{R}} + k_{\text{NR}})$. It is found that both the positive and negative polaron show bright absorption features and photoluminescence from the relaxed-excited state (RES) to the polaron ground states (PGS), but it is an inefficient process ($\text{PLQY} \sim 10^{-4}\text{--}10^{-7}$). Methodology considerations for improving the computed PLQY of polaron emission are discussed, such as Marcus rate corrections and coherence. This work provides computational support for observation of IR polaron absorption and a potential direction toward extending the emission capabilities of APbX_3 perovskites into the mid-IR to far-IR regime.



I. INTRODUCTION

The performance of solid-state optoelectronic devices, such as photovoltaic cells, light-emitting diodes (LEDs), lasers, and quantum computers, depends on factors such as the ground-state electronic structure of a material, the radiative and nonradiative dynamics of charge-carriers in the excited-state, light–matter interactions, and the interaction between interfaces of layers of materials in a device. Engineering the performance of these devices requires knowledge on how to tune features of electronic structures (i.e., band gap engineering) which are favorable for a desired purpose, such as maximizing the absorbance power density in photovoltaics, and alter the rates of excited-state processes, such as using confinement to enhance radiative recombination kinetics of charge-carriers for LEDs.

In the context of using solid-state materials as light emission sources, there are three primary regimes of interest: ultraviolet, visible, and infrared (IR). Here we will focus on infrared

emission sources. Utilizing IR electronic transitions within solid-state materials, as compared to thermal IR emission from vibrational modes, is beneficial since they have resonances which provide narrow-band emission while vibrational transitions provide broad-band emission. Within the IR spectrum there are four distinct regions: 700 nm–1.5 μm near IR (NIR), 1.5 μm –3 μm small wave IR (SWIR), 3 μm –8 μm medium wave IR (MWIR), and 8 μm –15 μm long wave IR (LWIR). Within the NIR and SWIR region the most common application for IR emission is for low loss telecommunications. For MWIR and LWIR the most common use is for thermal imaging and tracking.

The quantum efficiency of emission depends on the ratio of radiative and nonradiative recombination rates. The rates of

Received: August 23, 2019

Revised: October 27, 2019

Published: October 28, 2019

nonradiative recombination are expected to grow exponentially as the transition energy between electronic states approaches zero, by so-called “gap-law”.¹ This is a common constraint when trying to rationally design efficient IR PL sources. To obtain efficient IR photoluminescence (PL), three criteria are needed: (i) transition energies within the range of 0.1 to 1.8 eV, (ii) fast radiative recombination, and (iii) slow nonradiative recombination. Traditionally, transition energies tuned for IR PL have been obtained by utilizing the intrinsic bandgap of a material, using electronic confinement to tune the bandgap,² using heterostructures to tune the transition energy,³ and using doping to tune the bandgap.⁴ Recently, creating surface defect states has shown the ability to controllably tune the transition energy.⁵ Increasing the rates of radiative recombination can be achieved by increasing the exciton binding energy through electronic confinement⁶ or dielectric confinement.⁷ Slowing down nonradiative recombination rates can be accomplished by reducing the interaction of an excited-electronic state with its external environment, such as reducing temperature or using nanostructures to suppress phonon modes.⁸

APbX₃ (A = Cs, methylammonium(MA), formadamidinium(FA); X = I, Br, Cl) lead halide perovskites belong to a class of materials that have shown promise for high efficiency LEDs^{9–14} and photovoltaics.^{15–25} It is interesting to note that PV efficiency can be tuned by morphology control of radiative recombination^{12–15} and interfacial engineering.^{16–19} Scanning tunneling microscopy (STM) experiments of lead halide perovskite help provide a more complete picture of these materials.²⁶

The reasons APbX₃ lead halide perovskites show high promise for next-generation devices are due to a combination of facile wet-chemical synthesis coupled with high defect tolerance, physical tunability in the form of nanostructures, such as nanocrystals²⁷ (NCs), nanowires,²⁸ thin-films,²⁹ and layered materials,³⁰ and exotic excited-state properties.³¹ In particular, thin-films of MAPbI₃ have shown unusual charge-carrier transport properties, such as long nonradiative recombination rates in polycrystalline samples with high-defect densities. Recent work has suggested that the extended nonradiative lifetimes could potentially be attributed to photoinduced large polaron formation due to the cooperative motion of A site cations within the perovskite which trap the charge carriers into separate positive (hole) and negative (electron) polaronic states.^{32–35}

Polarons, quasi-particles formed due to the static coupling of electronic and nuclear degrees of freedom described by the Fröhlich Hamiltonian,³⁶ are typically observed in polar crystals and have a range of sizes which are based on the strength of the electron–phonon coupling. The coupling parameter is generally referred to as α . Large α produces small polarons, which trap the charge carriers to a single site within the lattice, and smaller α produces large polarons, which trap the charge carrier across multiple unit cell lengths. Similar to other quasi-particles, polarons have an electronic structure with the lowest polaron energy state being the polaron ground-state (PGS) and the next highest energy state being the relaxed excited-state (RES).³⁷

Polarons are also expected to be optically active and display two contrasting absorption mechanisms: dipole-allowed within the polaron potential well which requires conservation of angular momentum $\Delta l = \pm 1$ and photoionization of the bound polaron into the conduction/valence band continuum with a

transition energy threshold $\hbar\omega = 3E_p$, where E_p is the polaron binding energy.³⁸ Optical transitions within the polaron potential are defined by discrete, atomic like resonant transitions which scale with the binding energy E_p . This means that small polarons (large E_p) display higher energy transitions than large polarons (smaller E_p). Signatures of polaron photoionization are an absorption maximum near the threshold energy $\hbar\omega = 3E_p$ with an asymmetric tail toward the higher energy transitions. Recent transient absorption experiments have explored the optical response of excited-states in films of MAPbI₃ and observed IR absorption characteristics which were attributed to photoionization of large polarons into the continuum band states.^{39,40} Only recently have there been theoretical models developed toward predicting the role of negative and positive polarons on the radiative recombination in perovskites.^{41,42} Here we will use atomistic based models to compute the dipole-allowed transitions within the potential well for individual negative or positive polarons.

Large polarons in APbX₃ perovskites have the necessary energy spectrum to be IR photoluminescence (PL) sources. Considering that absorption and emission are inverse processes (i.e., the transition dipole operator is Hermitian), it seems conceivable to obtain IR PL from large polarons. The efficiency of IR PL would be determined by the kinetics of radiative and nonradiative recombination. Interestingly, polarons are known for screening phonons which slows down nonradiative transitions. Also, in a previous computational modeling work we reported slow hot-carrier cooling in the conduction band of a CsPbBr₃ NC atomistic model due to large spin–orbit coupling interaction and strong electronic confinement.⁴³ With the combination of a low conduction band DOS, large subgaps, and phonon-screening due to polaron formation, it seems possible that radiative recombination can be competitive with nonradiative recombination within the polaron potential well. Continuing from previous work, here we use density functional theory (DFT) based computational methodology^{44,45} to model the excited-state dynamics of hot-polarons in an atomistic CsPbBr₃ NC to test if polarons can be a potential IR PL source.

There are two mechanisms for the creation of polaronic states: a photoexcitation producing a simultaneous hole (positive) and electron (negative) or selective charge injection producing single polarons or bipolarons with the same charge. Once the charges are introduced to the lattice, polaron formation can be described by the static coupling of electronic and nuclear degrees of freedom within the Born–Oppenheimer (BO) approximation (diagonal matrix elements of the BO Hamiltonian).

To describe nonradiative polaron dynamics, one has to go beyond the Born–Oppenheimer approximation by accounting for the influence of nuclear kinetic energy during the propagation of electronic degrees of freedom. One of the most common approaches for accomplishing this is based on computing nonadiabatic couplings (NACs). NACs describe coupling of orthogonal electronic states due to electron–phonon interactions and can be converted into the analysis of phonon-assisted nonradiative transitions between electronic states. NACs can be computed with normal-mode analysis by explicitly solving for eigen-frequencies and eigen-modes⁴⁶ or using a molecular dynamics based on the “on-the-fly” approach.⁴⁷

Absorption and emission properties of polarons can be analyzed using the concept of transition dipoles, which

describe the coupling of electronic degrees of freedom to electromagnetic waves. As a first order approximation, optical transitions between electronic states can be considered in the independent orbital approximation (IOA)^{48,49} which neglects the Coulombic correlation between photoexcited electron–hole pairs. The IOA can be considered as a good approximation for two reasons: (i) for spatially confined materials, such as NCs, the orbital kinetic energy is more significant than the Coulomb potential energy⁵⁰ and (ii) perovskites show a very large photoinduced dielectric constant⁵¹ ($\epsilon_0 \approx 1000$) which effectively screens (reduces) Coulomb interactions. Higher order analysis of optical transitions, including the photoexcited electron–hole Coulomb interaction, requires computing transition densities using methodologies such as linear response time-dependent DFT (TDDFT) or the Bethe–Salpeter equation.⁴⁶

The rest of the manuscript is arranged as follows:

(II) Methods, and some background definitions, which are included in order to avoid ambiguities in notations and in procedures of computing observables: - (i) Mixed Quantum-classical methodology to describe polaron formation; (ii) ground-state observables of positive and negative polarons; (iii) description of density matrix-based equation of motion for electronic degrees of freedom coupled to a nuclear bath; (iv) description of excited-state dynamics observables; (v) computational details and description of the atomistic model used. (III) Results – (i) ground-state electronic structure, polaronic absorption spectra, and radial distribution functional analysis of polaronic geometries; (ii) hot-polaron excited-state dynamics, which includes nonradiative cooling of the hot-polaron and radiative IR emission from the hot-polaron. (IV) Discussion – Observations of hot-polarons within the literature, impact of surface chemistry on the coupling of vibrational modes to the hot-polaronic electronic states, assumptions of our excited-state dynamics and mixed quantum-classical methodology and their potential impact on the computed observables.

II. METHODS

II.(i). Theory of Polaron Formation in Mixed Quantum-Classical Methodology. The static coupling of electronic and nuclear degrees of freedom which results in polaron formation is generally described by the Fröhlich Hamiltonian.³⁶ In eqs 1–4 the Fröhlich Hamiltonian is described in second quantization formalism

$$H_{\text{polaron}} = H_e + H_{ph} + H_{e-ph} \quad (1)$$

H_e is the on-site electronic energy, H_{ph} is the phonon energy, H_{e-ph} is the cross-term which described interaction between electronic and nuclear degrees of freedom.

$$H_e = \sum_{n,k,\sigma} \zeta_{nk\sigma} c_{nk\sigma}^\dagger c_{nk\sigma} \quad (2)$$

In eq 2 n , k , and σ represent band, crystal momentum, and spin indices with $c_{nk\sigma}^\dagger$ and $c_{nk\sigma}$ being the Fermionic annihilation and creation operators. $\zeta_{nk\sigma}$ is the on-site electronic energy matrix element.

$$H_{ph} = \sum_{q,\nu} \hbar \omega_{q\nu} a_{q\nu}^\dagger a_{q\nu} \quad (3)$$

In eq 3 q and ν represent phonon momentum and mode index with $\hbar \omega_{q\nu}$ being the phonon mode energy. $a_{q\nu}^\dagger$ and $a_{q\nu}$ are the

Boson creation and annihilation operators. For a spatially confined particle $k = 0$ and $q = 0$.

$$H_{e-ph} = \sum_{n,n',\nu,\sigma} \gamma_{nn'}(\nu) \omega_\nu c_{n'\sigma}^\dagger c_{n,\sigma} a_\nu + h. c. \quad (4)$$

Equation 4 describes the interaction of electronic degrees of freedom with nuclear degrees of freedom with $\gamma_{nn'}(\nu, k, \nu)$ being the matrix element. H_{e-ph} can be decomposed into two distinct interactions: a “static” interaction H_{e-ph}^{static} when $n = n'$ and a dynamic interaction $H_{e-ph}^{\text{dynamic}}$ when $n \neq n'$. H_{e-ph}^{static} corresponds to a change of nuclear coordinates along an adiabatic potential energy surface (PES) which results in a lowering of energy, analogous to Jahn–Teller distortions. $H_{e-ph}^{\text{dynamic}}$ corresponds to changes in occupations of electronic and nuclear states allowing for dissipative dynamics.

For practical implementation of eqs 1–4 and atomistic modeling, we use the following mixed quantum-classical methodology: (i) Electronic contributions H_e are treated quantum mechanically and modeled in terms of noncollinear spin DFT where the wave functions are constructed in the form of two-component spinor Kohn–Sham orbitals (SKSOs) $\varphi_i^{\text{SKSO}}(\vec{r})$. (ii) Nuclear contributions H_{ph} are described within the classical path approximation (CPA) where nuclear wave functions are approximated as delta functions $\phi_\nu(R_I) = \delta(R_I - \langle R_I \rangle)$ with $\langle R_I \rangle = \langle \phi_\nu | R_I | \phi_\nu \rangle$ being the expectation value of the nuclear position. Thus, the phonon part of the Hamiltonian is represented in terms of positions and momenta of nuclei for potential and kinetic energies. (iii) The response of nuclear potential energy to changes in electronic configuration and electronic transitions facilitated by nuclear motion, originating from electron–phonon interaction in eq 4 are discussed in what follows.

Noncollinear spin DFT^{52,53} is used as the electronic basis, and we include the spin–orbit coupling (SOC) interaction due to the large angular momentum of conduction band Pb²⁺ 6p orbitals. A self-consistent noncollinear spin DFT uses four densities $\rho_{\sigma\sigma'}(\vec{r})$ and rests on the KS equation

$$\sum_{\sigma'=\alpha,\beta} (-\delta_{\sigma\sigma'} \nabla^2 + v_{\sigma\sigma'}^{\text{eff}}[\rho_{\sigma\sigma'}(\vec{r})]) \varphi_{i\sigma}(\vec{r}) = \varepsilon_i \varphi_{i\sigma}(\vec{r}) \quad (5)$$

In eq 5, α and β are orthogonal spin indices, and $v_{\sigma\sigma'}^{\text{eff}}[\rho_{\sigma\sigma'}(\vec{r})]$ is the 2×2 matrix operator of the effective potential. In accordance with the self-consistent Kohn–Sham theorem, the 2×2 effective potential is a functional of the electronic density for a N electron system $v_{\sigma\sigma'}^{\text{eff}} = \frac{\delta E^{\text{TOT}}[\rho_{\sigma\sigma'}^N]}{\delta \rho_{\sigma\sigma'}^N}$. The spin-dependent electronic density $\rho_{\sigma\sigma'}$ is dependent on the total number of electrons N . The total energy of the system $E^{\text{TOT}}[\rho_{\sigma\sigma'}^N]$ consequently depends on the number of electrons and determines the equilibrium ground state geometry when $\frac{\delta E^{\text{TOT}}[\rho_{\sigma\sigma'}^N]}{\delta R} = 0$ with R representing nuclear degrees of freedom.

For the N electron system the equilibrium bond distances will have distance R_{equilib}^N . Changing the total number of electrons $N \pm \Delta N$ changes the forces acting on nuclei $\frac{\delta E^{\text{TOT}}[\rho_{\sigma\sigma'}^{N \pm \Delta N}]}{\delta R}$ due to having a new electronic density $\rho_{\sigma\sigma'}^{N \pm \Delta N}$. For polaronic models with added/removed charge the equilibrium bond distances will be altered to give an updated equilibrium geometry $R_{\text{equilib}}^{N \pm \Delta N}$.

Solutions of eq 5 produce spinor Kohn–Sham orbitals (SKSOs) which are two component wave functions composed as a superposition of α and β spin components.

$$\varphi_i^{SKSO}(\vec{r}) = \begin{cases} \varphi_{i\alpha}(\vec{r}) \\ \varphi_{i\beta}(\vec{r}) \end{cases} = \varphi_{i\alpha}(\vec{r})|\alpha\rangle + \varphi_{i\beta}(\vec{r})|\beta\rangle \quad (6)$$

As a starting point, we determine the optimized geometry of the charge neutral model, in the absence of polarons, within the self-consistent DFT with N number of electrons. This corresponds to transforming the Fröhlich Hamiltonian terms in [eqs 2–4](#) to our mixed quantum-classical methodology.

$$H_e^N(r) + H_{ph}(R) + H_{e-ph}^{static}(r, R) = H_{SKSO}^N(r; R) \quad (7)$$

$H_{SKSO}^N(r; R)$ describes the electronic and nuclear degrees of freedom where the total energy depends parametrically on the nuclear coordinates R . This defines finding the minima of the PES with nuclear coordinates $R_{equilib}^N$ for the N electron system. We use this as a reference state to compare N electron system observables, such as equilibrium bond distances $R_{equilib}^N$, to the polaronic models.

To describe polaronic states we first add/remove charge ΔN from the N electron system to give a total of $N \pm \Delta N$ electrons. Then we do not allow the ions to reorganize around the new charge density $\rho_{\sigma\sigma'}^{N \pm \Delta N}$ keeping the nuclear coordinates fixed from the N electron system

$$H_e^{N \pm \Delta N}(r) + H_{ph}(R) + H_{e-ph}^{static}(r, R) = H_{SKSO}^{N \pm \Delta N}(r; R) \quad (8)$$

which is analogous to a Franck–Condon transition from the ground-state PES to the lowest-excited state PES.

Next, we allow the nuclei to reorganize around the charge density $\rho_{\sigma\sigma'}^{N \pm \Delta N}$ with change in nuclear coordinates δR

$$\begin{aligned} H_e^{N \pm \Delta N}(r) + H_{ph}(R) + H_{e-ph}^{static}(r, R) \\ = H_{SKSO}^{N \pm \Delta N}(r; R + \delta R) \end{aligned} \quad (9)$$

This term describes finding the minima of the lowest-excited state PES with nuclear coordinates $R_{equilib}^N + \delta R = R_{equilib}^{N \pm \Delta N}$. To approximate the electron–phonon interaction from the Fröhlich Hamiltonian, [eq 4](#), we subtract [eq 8](#) from [eq 9](#)

$$H_{e-ph}^{N \pm \Delta N}(r, R) = H_{SKSO}^{N \pm \Delta N}(r; R + \delta R) - H_{SKSO}^{N \pm \Delta N}(r; R) \quad (10)$$

which describes the reorganization energy from the Franck–Condon states on the excited-state PES to the minima of the excited-state PES.

II.(ii). Theory—Ground-State Observables. For each model we computed the electronic density of states DOS as

$$DOS_{SKSO} = \sum_i \delta(\epsilon - \epsilon_i^{SKSO} - \epsilon_{Fermi}) \quad (11)$$

with ϵ_i^{SKSO} being the band eigen-energies and ϵ_{Fermi} being the Fermi level $\epsilon_{Fermi} = \frac{\epsilon_{i,SKSO,HOMO} + \epsilon_{i,SKSO,LUMO}}{2}$

To quantify the changes in bond distances between ions, we compute radial distribution functions (RDFs) as

$$RDF(r) = \frac{1}{4\pi r^2} \sum_{IJ} \delta(r - |\vec{R}_I - \vec{R}_J|) \quad (12)$$

where $|\vec{R}_I - \vec{R}_J|$ represents the pairwise distance between ion I and J .

To dynamically couple electronic and nuclear degrees of freedom, we use adiabatic molecular dynamics (MD). This

provides kinetic energy of nuclei to break orthogonality of electronic states. Again, the nuclear degrees of freedom are treated in the CPA approximation with the nuclei following the classical path trajectories. The initial velocities of nuclei are scaled to keep a constant temperature, [eq 13](#), with forces acting on the nuclei depending on the electronic density $\rho_{\sigma\sigma'}^{N \pm \Delta N}$, [eq 14](#).

$$\sum_{I=1}^{N^{ion}} \frac{M_I}{2} \left(\frac{d\vec{R}_I}{dt} \Big|_{t=0} \right)^2 = \frac{3}{2} N^{ion} k_B T \quad (13)$$

$$\frac{d^2}{dt^2} \vec{R}_I = \vec{F}_I(\hat{\rho}_{\sigma\sigma'}^{N \pm \Delta N}) / M_I \quad (14)$$

\vec{R}_I represents ionic coordinates, M_I mass of the I^{th} nuclei, k_B is the Boltzmann constant, T is temperature, and $\vec{F}_I([\hat{\rho}])$ is the force acting on the ions which we specify is a functional of the electronic density $\rho_{\sigma\sigma'}^{N \pm \Delta N}$.

II.(iii). Theory—Reduced Density Matrix Equation of Motion for Electronic Degrees of Freedom. The time evolution of electronic degrees of freedom that are weakly coupled to a thermal bath can be described using the Redfield quantum master equation^{54,55} in the density matrix formalism.

$$\frac{d}{dt} \hat{\rho} = -\frac{i}{\hbar} \sum_k (F_{ik} \rho_{kj} - \rho_{ik} F_{kj}) + \left(\frac{d\rho_{ij}}{dt} \right)_{diss} \quad (15)$$

where F is the many-electron Fock matrix, which includes exchange and correlation, and ρ is the density matrix. The first term is the Liouville–von Neumann equation describing the unitary time evolution of a closed system while the second term describes electronic energy dissipation due to weak coupling to a thermal bath. The dissipative transitions result from the quantum part of the nuclear kinetic energy. The dissipative transitions are parametrized from NACs computed “on-the-fly” on the basis of SKSO orbitals

$$\begin{aligned} \hat{V}_{ij}^{NA}(t) &= -i\hbar \sum_I \left\langle \varphi_i^{SKSO}(\vec{r}, \{\vec{R}_I(t)\}) \left| \frac{\partial}{\partial \vec{R}_I} \right| \right. \\ &\quad \times \left. \varphi_j^{SKSO}(\vec{r}, \{\vec{R}_I(t)\}) \right\rangle \frac{\partial}{\partial t} \vec{R}_I \\ &= -i\hbar \left\langle \varphi_i^{SKSO}(\vec{r}, \{\vec{R}_I(t)\}) \left| \frac{\partial}{\partial t} \right| \varphi_j^{SKSO}(\vec{r}, \{\vec{R}_I(t)\}) \right\rangle \\ &= -\frac{i\hbar}{2\Delta t} \int d\vec{r} \left\langle \varphi_{i\alpha}^*(\vec{r}, \{\vec{R}_I(t)\}) \varphi_{i\beta}^*(\vec{r}, \{\vec{R}_I(t)\}) \right. \\ &\quad \left. \left\{ \varphi_{j\alpha}(\vec{r}, \{\vec{R}_I(t+\Delta t)\}) \right. \right. \\ &\quad \left. \left. \left. \varphi_{j\beta}(\vec{r}, \{\vec{R}_I(t+\Delta t)\}) \right\} + h. c. \right\rangle \end{aligned} \quad (16)$$

We highlight that in the limit of $\Delta t \rightarrow 0$ this expression reduces to the orthogonality relation $\delta_{ij} = \begin{cases} 1, & i = j \\ 0, & i \neq j \end{cases}$. Due to nuclear kinetic energy of nuclei the orthogonality relation is broken and provides a “mixing” of SKSOs. NACs are converted into rates of transitions by taking the Fourier transform of the autocorrelation function, [SI eqs 1a–1c](#), which provides components for the Redfield tensor R_{ijk} , [SI eq 1d](#). The Redfield tensor controls dissipative dynamics of the density matrix, [SI eq 2](#).

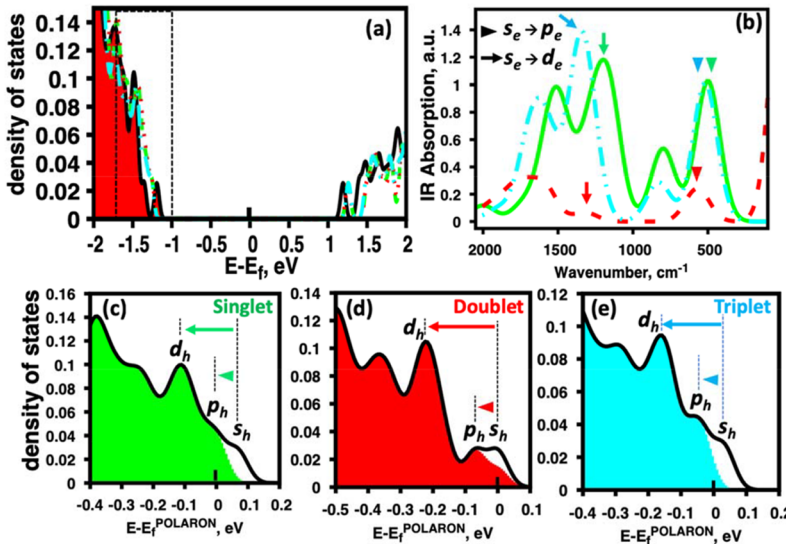


Figure 1. DOS and IR polaron absorption spectra for the positive polaron models. (a) DOS, aligned with the Fermi level of the neutral model, of four respective models: neutral perovskite NC (black, solid), positive polaron in singlet configuration (green, dashed), in doublet configuration (red, dash-dot), and triplet configuration (blue, dot-dash-dot). The boxed region is to highlight that we focus on the valence band DOS to observe positive polaron formation. (b) IR absorption spectra, computed using eq 20, spectra for the positive polaron plotted in units of wavenumbers for singlet (green, solid), doublet (red, dashed), and triplet (blue, dot-dot-dash) spin configurations. The inset triangles/arrows indicate $s_h \rightarrow p_h$ and $s_h \rightarrow d_h$ optical transitions which are illustrated in (c)–(e). DOS for the (c) singlet, (d) doublet, and (e) triplet polaron model. The energy axis is aligned to the Fermi level of the polaron. Shaded regions correspond to occupied states while white regions correspond to unoccupied states which we call the positive polaron. The s_h , p_h , and d_h labels indicate symmetry of the envelope function for those respective bands. For (c) and (e) the lowest energy optical transition is of $s_h \rightarrow p_h$ type while (d) is $s_h \rightarrow s_h$ type due to each band being 2-fold degenerate.

Dissipative transitions are treated perturbatively to second order with respect to the electron–phonon interaction and can be interpreted as state-to-state transitions analogous to Fermi’s Golden Rule. From the Redfield tensor R_{ijkl} we can approximate a nonradiative recombination rate k_{nr} from the polaron RES to PGS from the corresponding Redfield matrix elements

$$k_{nr} \approx R_{RES-PGS} \quad (17)$$

II.(iv). Theory—Excited-State Observables: Charge Distributions, Rates, Absorption Spectra, Photoluminescent Quantum Yields. We use the independent orbital approximation (IOA) where excited-states are described as a pair of orbitals, as opposed to a superposition of orbitals commonly used in TDDFT or Bethe-Salpeter approaches. Optical transitions between SKSO i and j can be found through transition dipole matrix elements, eq 18, which can be used to compute oscillator strengths, eq 19.

$$\langle \vec{D}_{ij} \rangle = e \int d\vec{r} \{ \varphi_{i\alpha}^* \varphi_{j\beta}^* \} \vec{r} \begin{Bmatrix} \varphi_{j\alpha} \\ \varphi_{j\beta} \end{Bmatrix} \quad (18)$$

$$f_{ij} = |\vec{D}_{ij}|^2 \frac{4\pi m_e v_{ij}}{3\hbar e^2} \quad (19)$$

With known oscillator strengths, an absorption spectrum can be computed through eq 20

$$\begin{aligned} \alpha^{SKSO}(\varepsilon) &= \sum_{i \leq HO} \sum_{j \geq LU} f_{ij} \delta(\varepsilon - \Delta\varepsilon_{ij}) \\ &= \sum_{i < j} f_{ij} \delta(\hbar\omega - \hbar\omega_{ij}) \{ \rho_{ii}^{eq} - \rho_{jj}^{eq} \} \end{aligned} \quad (20)$$

Partial contributions of bright transitions from orbitals occupied at equilibrium $\rho_{ii}^{eq} \approx 1$, $i \leq HO$ to orbitals unoccupied at equilibrium $\rho_{jj}^{eq} \approx 0$, $j \geq LU$. Note that the $HO = N \pm \Delta N$ depends on the total charge of the model and will take different values for positive and negative polarons. Time-resolved emission in the excited-state can be found based on the presence of inverse occupations along the excited-state trajectory and the intensity of the oscillator strength between states i and j

$$E(\hbar\omega, t) = \sum_{j > i} f_{ij} \delta(\hbar\omega - \hbar\omega_{ij}) \{ \rho_{jj}(t) - \rho_{ii}(t) \} \quad (21)$$

An emission spectrum can be generated from integrating the time-resolved emission along the trajectory

$$E^{tot}(\hbar\omega) = \frac{1}{T} \int_0^T E(\hbar\omega, t) dt \quad (22)$$

Rates of radiative recombination k_r can be found from Einstein coefficients for spontaneous emission⁵⁶

$$k_r = A_{PGS-RES} = \frac{8\pi^2 v_{PGS-RES}^2 e^2}{\varepsilon_0 m_e c^3} \frac{g_i}{g_j} f_{PGS-RES} \quad (23)$$

$f_{PGS-RES}$ is the oscillator strength from the RES to the PGS, $v_{PGS-RES}^2$ is the transition frequency from the RES to the PGS, g_i is the degeneracy of the electronic state, and the rest of the variables represent the fundamental constants. From the radiative recombination rate k_r and k_{nr} we compute a PLQY

$$PLQY = \frac{k_r}{k_r + k_{nr}} \quad (24)$$

II.(v). Computational and Atomistic Details. From the bulk CsPbBr_3 crystal structure a $2 \times 2 \times 2$ unit cell was carved

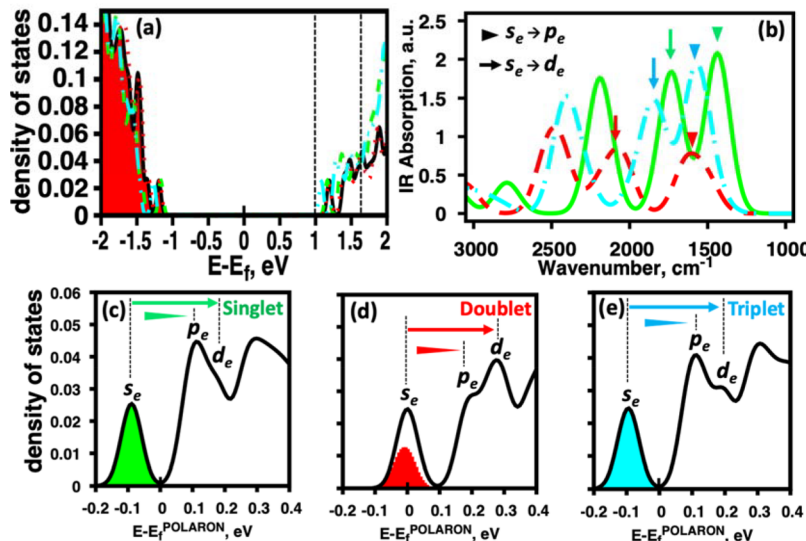


Figure 2. DOS and IR polaron absorption spectra for the negative polaron models. (a) DOS, aligned with the Fermi level of the neutral model, for the four respective models: neutral perovskite NC (black, solid), positive polaron in singlet configuration (green, dashed), in doublet configuration (red, dash-dot), and triplet configuration (blue, dot-dash-dot dot). The boxed region is to highlight that we focus on the conduction band DOS to observe negative polaron formation. (b) IR absorption spectra, computed using eq 20, spectra for the negative polaron, in units of wavenumbers, for singlet (green, solid), doublet (red, dashed), and triplet (blue, dot-dot-dash) spin configurations. The inset triangles/arrows indicate $s_e \rightarrow p_e$ and $s_e \rightarrow d_e$ optical transitions which are illustrated in (c)–(e). DOS for the (c) singlet, (d) doublet, and (e) triplet polaron model. The energy axis is aligned to the Fermi level of the polaron. Shaded regions correspond to occupied states while white regions correspond to unoccupied states. The occupied states are what we refer to as the negative polaron. The s_σ , p_σ , and d_σ labels indicate symmetry of the envelope function for those respective bands. For (c) and (e) the lowest energy optical transition is a $s_e \rightarrow p_e$ type while (d) is $s_e \rightarrow s_e$ type due to each band being 2-fold degenerate.

out giving Pb/Br terminated surfaces providing a composition of $\text{Cs}_8\text{Pb}_{27}\text{Br}_{54}$. To passivate terminal Pb^{2+} (Br^-) ions acetate anions (ethylammonium cations) are used as ligands and were coordinated to each respective surface atom.⁵⁷ Although previously published, the geometry of the model is illustrated in **SI Figure 1** Overall, this gives a structure of $\text{Cs}_8\text{Pb}_{27}\text{Br}_{54}$ passivated with 54 (48) acetate anions (ethylammonium cations) for a total of 995 ions and 2808 electrons. The original structure deviates from the ideal stoichiometry $\text{A}_x^{+}\text{B}_x^{2+}\text{C}_x^-$ which was fixed by charge balance to open the bandgap. This composition gives a NC that has an edge length of ~ 2 nm.

The ground-state electronic structure of our atomistic model was found using DFT with the generalized gradient approximation (GGA) Perdew–Burke–Ernzerhof (PBE) functional⁵⁸ in a plane-wave basis set along with projector augmented-wave (PAW) pseudopotentials^{59,60} in VASP⁶¹ software. We use a plane-wave cutoff of 400 eV and optimize the atomistic models until the forces on the atoms are less than 1 meV. From the ground-state nuclear configuration computed with the GGA functional, single point calculations were done using noncollinear spin DFT including the SOC interaction which was used to compute observables of the system. All calculations were performed at the Γ point. A simulation cell size of $31 \times 31 \times 31$ Å with 7 Å of vacuum in each direction was used. The charge neutral ground-state structure is optimized using the N electron system. To model polaron formation, we add/remove ΔN electrons from the system and reoptimize the structure. Illustration of this process is shown in **SI Figure 2(a)–(c)**. The spurious electrostatic interactions between replicas of charged species discussed by Neugebauer and Scheffler⁶² are avoided with the use of a background charge concept.⁶³

To explore the electronic and optical properties of various spin multiplicity polaronic states, we implement constrained

DFT. Within spin-polarized DFT we specify the number of α and β electrons from the spin-dependent electronic density ρ_σ to have $N_\alpha = \int \rho_\alpha dr^3$ and $N_\beta = \int \rho_\beta dr^3$. Their difference $\delta N = N_\alpha - N_\beta$ defines the spin state $s = \frac{\delta N}{2}$ and multiplicity $m = 2s + 1$.⁶⁴ We explored singlet ($m = 1$), doublet ($m = 2$), and triplet ($m = 3$) spin multiplicities. Note that $N_\alpha + N_\beta$ defines the total number of electrons and is different for positive and negative polarons. The noncollinear spin DFT charge density was constrained to have a specified multiplicity from the spin-polarized charge density.

To initialize MD, the NC model was set to a Nose–Hoover thermostat and heated to 300 K. Once temperature was reached, the MD trajectory was propagated for 1 ps using $\Delta t = 1$ fs time steps under the NVT ensemble.

III. RESULTS

III.(i). Polaron Ground-State Electronic Structure and Radial Distribution Functions. In **Figure 1(a)–(e)** we show the density of states (DOS) of each spin multiplicity and their IR absorption spectra for the positive polaron model. **Figure 1(a)** shows the DOS of the ground-state model (black) singlet (green, dashed), doublet (red, dashed), and triplet (blue, dot-dashed) with the Fermi energy being aligned with the neutral ground-state model. The boxed region of the valence band corresponds to the location of the positive polarons in the DOS. Filled in regions of the curve correspond to occupations, and for clarity we only show ground-state occupations for **Figure 1(a)**. **Figure 1(b)** shows the IR absorption spectra for singlet (green, solid), doublet (red, dashed), and triplet (blue, dot-dash-dot) polaron models. It is observed that the singlet and the triplet lowest energy transition are of high intensity compared to the doublet. **Figure 1(c)–(e)** shows the positive polaron DOS for the (c) singlet, (d) doublet, and (e) triplet models with the energy axis being aligned to the polaron Fermi

level for each respective model. Filled in regions of Figure 1(c)–(e) correspond of occupied states with white regions being unoccupied hole states which we refer to as positive polarons. The s_h , p_h , and d_h labels indicate interpretation of symmetry of the envelope function for those respective bands. A comment on rigorous definition of these labels is provided in the SI. For the singlet and triplet polarons Figure 1(c) and (e) it is observed that the Fermi energies align in-between the s_h and p_h bands while for the doublet Figure 1(d) it is aligned with the s_h band. This is due to each band being twice degenerate^{31,65} for APbX_3 perovskites. This also means that the lowest energy optical transitions for (c) and (e) are $s_h \rightarrow p_h$ types of transitions while (d) is of $s_h \rightarrow s_h$ type. In Figure 1(b) the inset arrows indicate $s_h \rightarrow p_h$ IR optical transitions for each model.

In Figure 2(a)–(e) we show the DOS and IR absorption spectra for negative polaron models which has the same format as Figure 1(a)–(e). Figure 2(a) shows the DOS of the ground-state model (black) singlet (green, dashed), doublet (red, dashed), and triplet (blue, dot-dashed) negative polarons with the Fermi energy being aligned with the neutral ground-state model. The boxed region of the valence band corresponds to the location of the negative polarons in the DOS. Figure 2(b) shows the IR absorption spectra for singlet (green, solid), doublet (red, dashed), and triplet (blue, dot-dashed) polaron models. It is observed that the singlet and the triplet lowest energy transition are of high intensity compared to the doublet. It is also observed that in Figure 2(b) the negative polaron spectrum is of higher intensity than Figure 1(b) the positive polaron spectra. Figure 2(c)–(e) shows the negative polaron DOS for the (c) singlet, (d) doublet, and (e) triplet model with the energy axis being aligned to the polaron Fermi level for each respective model. Filled in regions of Figure 2(c)–(e) correspond of occupied states, which we refer to as the negative polaron, with white regions being unoccupied hole states. The s_o , p_o , and d_o labels indicate symmetry of the envelope function for those respective bands. The alignment of polaron Fermi levels in Figures 2(c)–(e) follows the same trends as Figure 1(c)–(e). This again means that the lowest energy optical transitions for Figures 2(c) and (e) are $s_h \rightarrow p_h$ types of transitions while (d) is of $s_h \rightarrow s_h$ type. In Figure 2(b) the inset arrows indicate $s_h \rightarrow p_h$ IR optical transitions for each model.

The PGS optimized geometry is expected to be different than the neutral QD ground state geometry due to static coupling of electronic and nuclear degrees of freedom, in accordance with the Fröhlich Hamiltonian, eqs 1–4, and its quantum-classical approximation, eqs 7–10. In Figure 3(a)–(f) we quantify the difference between geometries by plotting RDFs, eq 12. RDFs compare pairwise distances between ions and serve as a measure of changes in geometry due to polaron formation. Figure 3(a), (c), and (e) show RDFs for positive polarons and (b), (d), and (f) for negative polarons with (a)–(b) comparing Pb–Br and Br–Br distances labeled with peaks A/A' and B/B', (c)–(d) comparing Cs–Br distances labeled with peaks C/C', and (e)–(f) comparing Cs–Pb pairwise distances labeled with peaks D/D' and E/E'. For each plot in Figure 3(a)–(f) the RDF is plotted for the optimized, neutral ground state (black, solid), singlet (green, dash–dash), doublet (red, dot-dot), and triplet (blue, dot-dash) spin configuration for the optimized polaron geometries. Increases (decreases) in peaks of the RDF between the neutral ground state and PGS can be associated with increases (decreases) in coordination

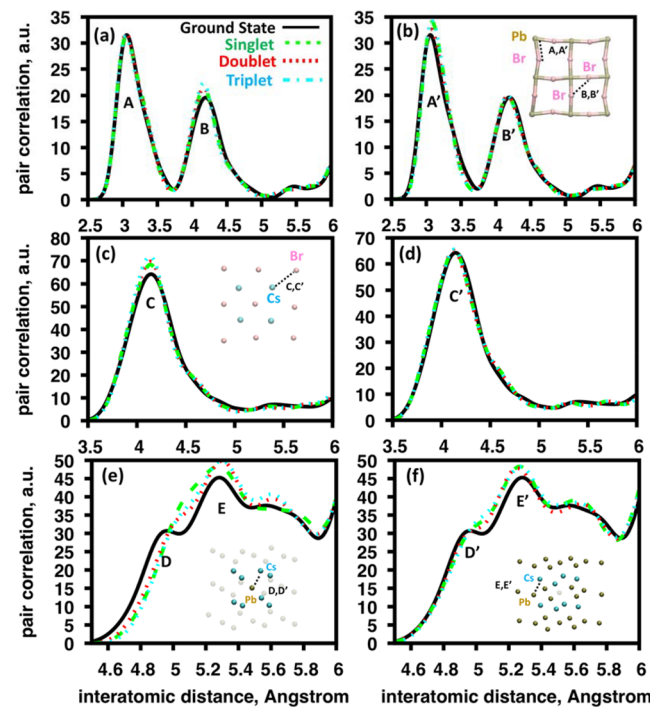


Figure 3. Distributions of pairwise distances, computed using eq 12, between (a)–(b) Pb–Br signified with the A/A' peak and Br–Br distance represented with B/B', (c)–(d) Cs–Br represented with peak labels C/C', and (e)–(f) Cs–Pb ions represented with peak labels D/D' and E/E'. (a), (c), and (e) are RDFs for positive polarons and (b), (d), and (f) for negative polarons. For all plots, RDF is plotted for the optimized, neutral ground state (black, solid), singlet (green, long-dash), doublet (red, short-dash), and triplet (blue, dot-dash-dot-dot) spin configuration for the optimized polaron geometries. Insets for (b), (c), (e), and (f) illustrate the bond distances that are being computed for the labeled peaks. We note that peaks D/D' indicate distances between the interior Pb^{2+} ion and Cs^+ ions while the E/E' peaks are between surface Pb^{2+} ions and Cs^+ ions.

number of ions⁶⁶ due to polaron formation. Shifts in RDF peaks along the x -axis would correspond to average bond/coordination elongation or contraction. Numerical values of the peaks labeled in Figures 3(a)–(f) are shown in Table 1.

Comparing Pb–Br and Br–Br bond distances in Figure 3(a) positive polaron and (b) negative polaron RDF to the NGS, it is observed that (a) shows an increase in the feature B along with bond contraction while (b) shows an increase in feature A' with a bond elongation. This indicates that the positive polaron increases coordination between Br ions while the negative polaron increases coordination between Pb–Br ions. When considering that the conduction (valence) band edges are composed of Pb^{2+} 6p (Br^- 4p) states, the addition (removal) of charge is reducing (oxidizing) the system. For the negative polaron model this would imply that the oxidation state will fractionally change to $\text{Pb}^{(2-\delta)+}$ which will decrease the electrostatic attraction between Pb and Br ions resulting in an elongated bond length (feature A' in Figure 3(b)). We note the same trend in Pb–Br bond elongation has been observed elsewhere for CsPbBr_3 atomistic models.^{35,67} For the positive polaron, an electron is being removed from the valence band edge which fractionally decreases the electronegativity $\text{Br}^{(1-\delta)-}$. This would decrease the electrostatic repulsion between nearest neighbor Br ions and decrease the coordination distance between them (feature B in Figure 3(a)). Decreased

Table 1. Maxima, r_{\max} , and FWHM of Peak Features RDF Functions Shown in Figure 1^a

	Singlet		Doublet		Triplet	
	r_{\max} [Å]	fw hm [Å]	r_{\max} [Å]	fw hm [Å]	r_{\max} [Å]	fw hm [Å]
Positive Polaron						
A [r(Pb–Br)]	3.04 (−0.02)	0.46 (+0.01)	3.05 (−0.01)	0.46 (+0.01)	3.04 (−0.02)	0.47 (+0.02)
B [r(Br–Br)]	4.17 (−0.02)	0.44 (−0.05)	4.17 (−0.01)	0.44 (−0.05)	4.16 (−0.03)	0.42 (−0.07)
C [r(Cs–Br)]	4.14 (0)	0.51 (−0.03)	4.13 (−0.01)	0.49 (−0.05)	4.13 (−0.01)	0.48 (−0.06)
D [r(Pb–Cs)]	x	x	x	x	x	x
E [r(Pb–Cs)]	5.27 (−0.01)	x	5.30 (+0.02)	x	5.30 (+0.02)	x
Negative Polaron						
A' [r(Pb–Br)]	3.08 (+0.02)	0.42 (−0.03)	3.07 (+0.01)	0.44 (−0.01)	3.08 (+0.02)	0.42 (−0.03)
B' [r(Br–Br)]	4.16 (−0.03)	0.49 (0.00)	4.17 (−0.02)	0.49 (0.00)	4.16 (−0.03)	0.48 (−0.01)
C' [r(Cs–Br)]	4.13 (−0.01)	0.54 (0.00)	4.12 (−0.02)	0.55 (+0.01)	4.13 (−0.01)	0.55 (+0.01)
D' [r(Pb–Cs)]	x	x	x	x	x	x
E' [r(Pb–Cs)]	5.26 (−0.02)	x	5.25 (−0.03)	x	5.25 (−0.03)	x

^aFeatures A–E correspond to the positive polaron while features A'–E' correspond to the negative polaron. The parentheses indicate the difference between r_{\max} and FWHM from the ground state and the respective polaron state. 'x' value in the table indicates undefined values. D[r(Pb–Cs)] peak appears for the ground state geometry but broadens and loses a defined peak for polaronic geometries.

Br–Br coordination also suggests that under oxidation the octahedral Pb–Br lattice undergoes greater tilting and reduces the connectivity between adjacent octahedra.

Cs–Br bond distances only show significant changes for the Figure 3(c) positive polaron formation while (d) negative polaron formation shows negligible change in RDF. Figure 3(c) peak C shows an increase in coordination between Cs and Br ions and elongation of pairwise distances. Again due to positive polaron formation the Br ions will have a decreased electronegativity $\text{Br}^{(1-\delta)-}$ and have a decreased Coulombic attraction to positive Cs^+ ions. This would account for the decrease in pairwise distances.

Coordination between Cs–Pb ions shown in Figure 3(e)–(f) shows two peaks. The D/D' peaks are attributed to coordination of Cs^+ to the interior Pb^{2+} ion (center of the $2 \times 2 \times 2$ unit cell structure), and the E/E' peaks are attributed to coordination of Cs^+ to exterior surface Pb^{2+} ions. Comparing the neutral ground state and polaron RDF for the D/D' peaks, it is observed that the peak broadens and no longer has a well-defined maximum while the E/E' peaks increase. This implies that the Cs^+ ions expand away from the center of the core toward the surface Pb^{2+} ions.

Changes in the RDF peak intensity can be related to an increase/decrease of crystallinity of the sample. Increases of intensity correspond to narrowing of the distribution (increased crystallinity) while decreases in intensity correspond to broadening of the distribution (reduced crystallinity). One can quantitatively access the measure of crystallinity by comparing full-width half-maxima (fw hm) for distributions before and after polaron formation. An ideal cubic phase provides Dirac delta functions for each bond/coordination distance. It is observed that the most significant changes in fwhm occur for the positive polaron model with a narrowing of features B and C in Figure 3, as observed in Table 1.

Observed quantitative changes in RDF are indeed small. However, hypothetical changes, such as breaking of one out of six Pb–Br bonds in an octahedral coordination would hypothetically lead to reducing of the heights of the relevant RDF peaks in proportion 5/6 while generating heights of 1/6 to an elongated coordinate compared to the original peak.

III.(ii). Polaron Excited-State Dynamics. For excited-state dynamics we focus on the singlet positive polaron and the singlet negative polaron which will be referred to as the

positive and negative polaron, respectively. To dynamically couple electron and nuclear degrees of freedom, we implement adiabatic molecular dynamics (MD) and use that trajectory to compute NACs which provide off-diagonal elements of the BO Hamiltonian. Fluctuations of SKSO energies along a 1 ps adiabatic molecular dynamics (MD) trajectory for positive and negative polarons are shown in SI Figure 3 and SI Figure 4, respectively. From the adiabatic MD trajectories, we compute NACs “on-the-fly” and use them to parametrize the Redfield equations, eqs 15–16, to generate state-to-state dissipative transitions, in the spirit of Fermi Golden Rule.

The rates of these state-to-state transitions are illustrated in Figure 4(a)–(b) in the form of Redfield tensors R_{ijj} for the positive polaron in (a) and the negative polaron in (b). The “Orbital i” and “Orbital j” axis represent states in the (a) conduction band and (b) valence and are labeled with the symmetry of their envelope function. The R_{ijj} axis represents the nonradiative state-to-state transition rate in units of ps^{-1} . These rates are used to compute dynamic nonradiative cooling rates k_{cooling} and nonradiative recombination rates k_{nr} . Note that only off diagonal tensor elements are nonzero while all diagonal elements are zero. For Figure 4(a)–(b) it is observed that there are alternating high intensity transitions near the main diagonal and numerous low intensity transitions away from the main diagonal. The altering high intensity transitions $R_{ii,i-1,i-1}(i) \approx R_0(\delta_{i+1,j} + \delta_{i,j+1}) \frac{1+(-1)^i}{2}$ are between near-degenerate states whose average band energies only deviate by a few millielectronvolts while the low intensity transitions are between bands whose average energy is within thermal energy kT . It is also observed that for Figure 4(b) the negative polaron transition rates are very low near the conduction band edge within the orbital range [LU, LU+12]. For a comparison of the Redfield tensors for the positive doublet and negative triplet and more detailed description of the Redfield tensor we refer readers to SI Figures 5–6.

The initial conditions for the dynamics simulation are interpreted as the following: the time scale of nuclear reorganization (i.e., polaron formation) $\tau_{\text{reorganization}}$ is much faster than the time scale of the charge-carrier dissipating its excess energy to the lattice as phonons $\tau_{\text{dissipation}}$. In other words, the excited-state trajectory corresponds to a hot-polaron within the self-trapped Coulomb potential well which

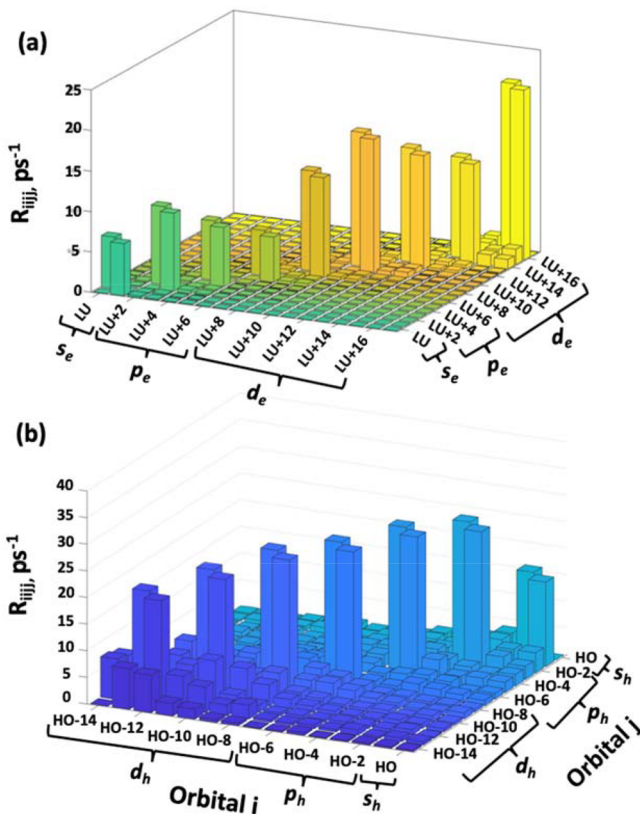


Figure 4. Redfield tensor (a) negative singlet polaron and (b) positive singlet polaron. The “Orbital i” and “Orbital j” axis represent states in the (a) conduction band containing symmetry states s_e [$LU, LU + 1$], p_e [$LU + 2, LU + 7$], and d_e [$LU + 8, LU + 17$] and the (b) valence band with envelope symmetry states s_h [$HO, HO - 1$], p_h [$HO - 2, LU - 7$], and d_h [$LU - 8, LU - 14$]. The R_{ijj} axis represents the nonradiative state-to-state transition rate in units of ps^{-1} . These rates are used to compute hot-carrier nonradiative cooling rates based on initial population conditions. It is observed that there are alternating high intensity transitions near the main diagonal and numerous low intensity transitions away from the main diagonal. The high intensity transitions are between near-degenerate states whose average band energies along the MD trajectory only deviate by a few millielectron-volts, while the low intensity transitions are between bands whose average energy is within thermal energy kT . Note that (b) the positive polaron model has higher intensity off-diagonal elements than (a) the negative polaron model. This indicates that the positive polaron has greater coupling to nuclear vibronic degrees of freedom.

dissipates energy to the surrounding heat bath. This results in hot-polaron cooling from the initial condition to the RES. We then compute the rate of hot-polaron cooling from the initial condition to the RES as a function of dissipation energy $E_{\text{diss}} = E_{\text{IC}} - E_{\text{RES}}$ where E_{IC} is the energy of the initially occupied hot-polaronic state and E_{RES} is the energy of the relaxed-excited state.

Figure 5(a)–(b) shows hot-carrier cooling along the excited-state trajectory (a) for negative polaron model and (b) positive polaron model from a nonequilibrium state to the polaron RES. The energy axis is in reference to the Fermi level of the polaron model with the time axis in log scale normalized to 1 ps. Green color code represents background reference charge density, yellow represents average occupation of charge density distribution in conduction band $\Delta n > 0$, and blue represents average occupation of charge density distribution in valence band $\Delta n < 0$. Horizontal dotted/solid lines represent

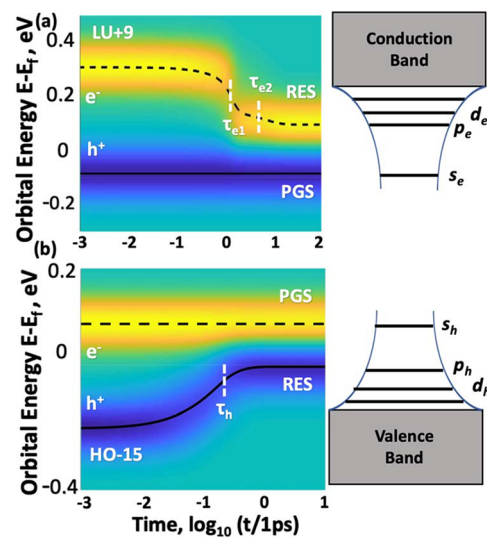


Figure 5. Hot-carrier cooling dynamics for (a) negative polaron and (b) positive polaron. The energy axis is in reference to the Fermi level for each polaron with the time axis in log scale normalized to 1 ps. Green represents background reference, yellow represents average occupation of charge density in conduction band, and blue represents average occupation of charge density in valence band. Horizontal dotted/solid lines represent energy expectation values of charge carriers, SI eq 3(c), and vertical dashed lines represent hot carrier cooling times τ_{cooling} fit to a single exponential decay, SI eq 4(a)–(b). The initial condition corresponds to a polaron with excess kinetic energy in the polaron potential well that then cools to the polaron RES (p_h/p_e). For (a) the carrier decay follows a biexponential decay while for (b) it is observed that the cooling follows closely to monoexponential decay. The biexponential decay is attributed to large subgaps, low density of states, and polaron screening of phonons which reduces NAC.

energy expectation values of charge carriers, SI eqs 3a–3c, and vertical dashed lines represent hot carrier cooling τ_{cooling} fit to a single exponential decay, SI eqs 4a–4b. Hot carrier cooling for positive doublet polaron and negative triplet polaron are shown in SI Figure 7 and explicit changes in occupations along the excited-state trajectory with normalized carrier-cooling curves $\rho_{ii}(t)$ are shown in SI Figure 8 and SI Figure 9, respectively.

For the negative polaron in Figure 5(a) it is observed that the hot-carrier shows a biexponential decay. The “fast” component has a lifetime around $\tau_{e_1} \approx 1$ ps, and the slow component has a lifetime on the order of $\tau_{e_1} \approx 10$ ps. This is also readily observed in SI Figure 9(a) when comparing the computed hot-carrier relaxation to the single exponential fit. For the positive polaron in Figure 5(b) it is observed that hot-carrier cooling follows closely to a single exponential decay with subpicosecond carrier cooling $\tau_h < 1$ ps. In Figure SI 10 we compare the cooling time of positive (red, large circle) and negative (green, small circle) hot-polarons cooling time to positive (black, small dot) and negative (blue, small dot) free-carriers as a function of dissipation energy E_{diss} . It is observed that it takes longer for the hot-polarons to dissipate their energy to the surrounding heat bath than if they were free-carriers. This can be attributed to the polaronic geometries resulting in Jahn–Teller like distortions which reduce nonadiabatic coupling between electronic states.

A competing mechanism for nonradiative electronic energy dissipation through phonons is dissipation in the form of

photons. A “hot” carrier can dissipate energy in the form of IR photons before relaxing to the RES giving IR PL. This is what we plot in Figure 6(a)–(d). Figure 6(a)–(b) show the (a)

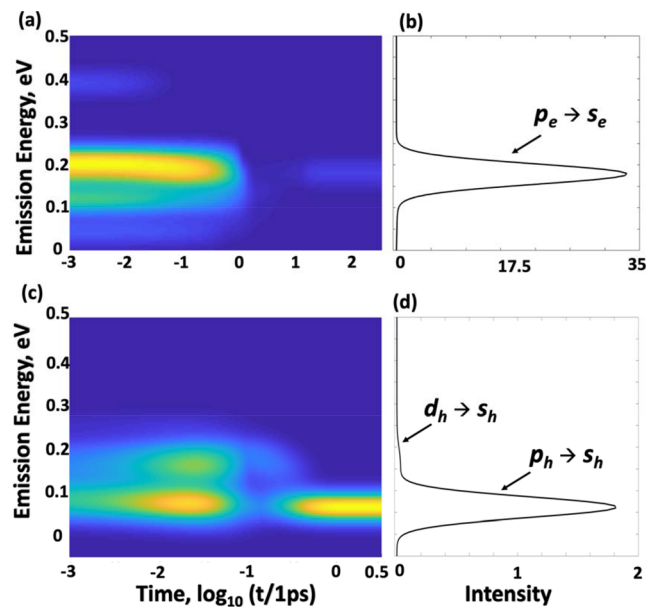


Figure 6. Radiative relaxation along the excited-state trajectory with (a), (c) showing time-resolved emission and (b), (d) showing time-integrated radiative emission for the (a)–(b) negative polaron and (c)–(d) positive polaron. The dynamics at this figure corresponds to the same initial conditions as Figure 5. Before cooling to the polaron RES hot carriers can emit IR photons to dissipate energy which competes with nonradiative transitions. Once cooled to the RES the polaron emits to the PGS. The trajectories were propagated for (a) 5 ps and (c) 500 ps in accordance to the nonradiative recombination rates, as seen in Table 2. In (a) and (c) the blue background represents optically “dark” states with colored regions indicating occupation of optically “bright” states with a population inversion, by eq 21. Yellow represents the most intense optical transitions along the excited-state trajectory. Figure 6(b) and (d) sum the optical transitions along the trajectory, by eq 22. For both models it is observed that there is cascading hot carrier emission before decaying to the RES giving polaron PL. Once cooled to the RES both models show $p_x \rightarrow s_x$ ($x = e, h$) transitions giving rise to IR PL which is greater in intensity than the hot carrier emission. It is observed that (b) the negative polaron has 1.5 orders of magnitude greater intensity than (d) the positive polaron. This is attributed to extended nonradiative lifetime of the negative polaron model, see Table 2.

time-resolved, eq 21, and (b) time-integrated emission, eq 22, for the negative polaron along the excited-state trajectory. Figure 6(c)–(d) show the same plots but for the positive polaron. In Figure 6(a) and (c) the time axis is in log scale

normalized to 1 ps. The electronic excited-state trajectories were propagated for (a)–(b) 5 ps and (c)–(d) 500 ps in accordance to the nonradiative recombination rates, as seen in Table 2. The blue background represents the “dark” reference states with colored regions indicating occupation of optically “bright” states with a population inversion and PL. Yellow represents the most intense optical transitions along the excited-state trajectory. Figure 6(b) and (d) show the time integrated PL spectrum.

For both Figure 6(a) and (c) it is observed that there is a cascade of “hot” emission events before cooling to the polaron RES. Once the hot-carriers cool to the RES, there is polaron PL from the RES to the PES arising from $p_e \rightarrow s_e$ and $p_h \rightarrow s_h$ transitions, respectively. From comparing (b) the negative polaron and (d) the positive polaron it is observed that that (b) has 1.5 order of magnitude larger intensity than (d). It is also noted that there is a weak $d_h \rightarrow s_h$ hot PL observed in (d). SI Figure 12(a)–(b) compares the integrated PL spectrum of Figure 6(b) and (d) to their respective absorption spectra from Figure 1(b) and 2(b). This provides support for the types of optical transitions observed in Figure 6(b) and (d).

To determine the efficiency of IR PL from the positive and negative polaron, we compute PLQY from k_r and k_{nr} . k_r is computed from oscillator strengths using the Einstein coefficient for spontaneous emission, eq 23, and k_{nr} is found from the corresponding Redfield tensor element $R_{RES-PGS}$, eq 17. Table 2 shows k_r , k_{nr} , and PLQY for models presented here. It is observed that the negative polaronic models show higher PLQYs than the positive polaron models with the negative singlet showing the highest computed PLQY on the order of 10^{-4} .

IV. DISCUSSION

The main observable of interest in this paper is the spectral properties of individual polarons in a CsPbBr_3 perovskite NC model. We also investigate the structural reorganization of the lattice due to static electron–phonon interactions and the emissive properties of the positive and negative polarons. Within the discussion section we expand on the following topics: correspondence between atomistic based modeling of polarons and relation of the excited-state dynamics of hot-carrier cooling simulations to experimental findings, the role of surface ligands on the excited-state dynamics, and comments on the assumptions and approximations of our methodology.

In our excited-state dynamics for a CsPbBr_3 NC we modeled the hot-carrier cooling of polarons with excess energy within the polaron potential well to the RES. This assumes that upon photoexcitation/charge injection that nuclear reorganization (static electron–phonon interaction) is much faster than energy dissipation (dynamical electron–phonon interaction),

Table 2. Oscillator Strength f_{ij} (eq 19), Radiative Recombination Rate k_r (eq 23) Nonradiative Recombination rate k_{nr} (eq 17), Resultant PLQYs for Each Model Study (eq 24), and the Logarithm of Each PLQY^a

Model	f_{ij}	k_r [1/ns]	k_{nr} [1/ns]	PLQY	$\log(\text{PLQY})$
Positive-Singlet	0.14	2.81×10^{-4}	2.08×10^3	1.35×10^{-7}	-7
Positive-Doublet	0.07	1.95×10^{-4}	6.30×10^3	3.09×10^{-8}	-8
Negative-Singlet	0.29	5.10×10^{-3}	1.64×10^1	3.11×10^{-4}	-4
Negative-Triplet	0.30	5.38×10^{-3}	4.34×10^3	1.24×10^{-6}	-6

^aThe negative singlet polaron shows 2 to 4 orders of magnitude greater PLQY than the other models with both the negative polaron models showing higher PLQY than the positive polaron models. This is attributed to the negative polaron models showing an order of magnitude faster k_r and the negative singlet having a 2 orders of magnitude reduced k_{nr} .

$\tau_{cool} \ll \tau_{reorganization}$. A recent transient absorption study seems to suggest that some varieties of $APbX_3$ perovskites are capable of forming hot-polaronic states. In a bulk crystal of the fully inorganic $CsPbBr_3$ it was observed that carrier cooling τ_{cool} occurs faster than polaron formation $\tau_{reorganization}$ while for $MAPbBr_3$ carrier cooling and polaron formation occur on the same time scale.⁶⁸ This suggests that cation engineering of the perovskite can possibly be used to prepare a hot-polaronic state before the carrier dissipates all of its excess energy to the lattice. Another parameter which may impact the relative time scales of τ_{cool} and $\tau_{reorganization}$ is the degree of quantum confinement within a nanostructure. Increasing confinement leads to sparse electronic states with large subgaps between states. Heuristically, increased confinement should slow down τ_{cool} and make $\tau_{reorganization}$ more competitive, allowing for more efficient hot-polaron formation.

Comparing hot-carrier cooling dynamics between the various $APbX_3$ is a challenging subject. Assuming low excitation densities, we identify four independent criteria of comparison: (1) nonadiabatic coupling (NAC) of free charges to lattice vibrations for each specific compound; (2) the rate of lattice reorganization and polaron formation after photo-excitation/charge injection for each compound; (3) NAC of bound polarons to lattice vibrations; (4) the dimensionality of the perovskite (bulk versus nanostructures) which will alter the frequencies and spatial pattern of lattice vibrations that couple to the polarons and/or free charges along with altering the energy spacing between band edge states. In the work presented here we attribute the observation of biexponential decay in the cooling dynamics to (3) and (4).

- (1) Calculations have shown that free-carriers in $CsPbBr_3$ display greater NAC than $CsPbI_3$ materials due to I^- having greater inertia than Br^- .⁶⁹ Experiments show that organic–inorganic perovskites are able to dissipate heat more readily than all inorganic Cs^+ based perovskites⁷⁰ indicating greater NAC.
- (2) Polaron formation requires the static coupling of vibrational modes to free charges. In $APbX_3$ perovskites the main contributions toward polaron formation will come from the reorganization of the PbX_6^{2-} inorganic octahedra and reorientation of the A^+ cations. One experiment seems to indicate that polaron formation rates are more strongly dependent on A^+ cation composition than halide content.⁶⁸
- (3) Once the lattice reorganizes around the free charge to produce a polaron, it is expected that the rates of relaxation (hot carrier cooling, radiative recombination, nonradiative recombination) will decrease due to decreased NAC (via screening of the polaron). Calculations suggest that polaron formation reduces heat dissipation leading to longer hot-carrier cooling times.⁷¹
- (4) Experimentally it is observed that perovskite quantum dots show slower hot-carrier cooling than their bulk counterparts of the same chemical composition.^{72–74} Computationally it was observed that bulk $MAPbI_3$ showed fast subpicosecond hot-carrier cooling.⁷⁵ In previous work we observed that for a strongly confined $CsPbBr_3$ NC carrier cooling displayed a biexponential decay due to a large subgap in the conduction band. This is related to the so-called “phonon bottleneck” mechanism.

To summarize, the biexponential decay is attributed to the large subgaps which slow the hot-electron cooling. Then with the explicit account for polaronic effects in the excited-state the hot-carrier cooling rates decrease compared to the rates for a free-carrier, see [SI Figure 10](#).

The negative polaron models show enhanced (2–4 orders of magnitude) PLQY compared to the positive polaron models. This can be attributed to the combination of the negative polarons model showing slightly faster radiative recombination rates and slower nonradiative recombination rates, observed from [Table 2](#). The faster radiative recombination rates of negative polarons can be attributed to the larger oscillator strengths and slightly larger transition energies. This explains the 0.5 order of magnitude difference between the negative and positive polarons radiative recombination rates. The difference in nonradiative rates requires more in-depth analysis.

To understand why the negative singlet polaron shows 2 orders of magnitude slower nonradiative recombination rate than the other models, we utilize vibrational modes analysis. According to the bilinear electron–phonon interaction in [eq 4](#), nonradiative relaxation of charge carriers requires a resonance between frequency of nuclear vibrational modes and energies of electronic transitions $\hbar\omega^{vib} \approx \epsilon_i - \epsilon_f$. To approximate the vibrational energy spectrum provided by the passivation ligands, we implement normal-mode analysis, [SI eq 6](#), on a 2-D film $Cs_8Pb_{12}Br_{32}$ passivated by the same ligands used for the NC model (shown in [SI Figure 13](#)). The 2-D film was used since normal-mode analysis for the full NC model was found to be prohibitively expensive in numerical resources.

[Figure 7\(a\)–\(c\)](#) compares (a) the vibrational modes to the IR spectra of the (b) negative polaron models and (c) positive polaron models. It is seen that for (c) the positive polaron model the lowest energy optical transitions fall in resonance with normal modes in the range of [1500, 500 cm^{-1}] while for (b) the negative polaron model has a “mismatch” between radiative transitions energies and vibrational transition energies within the range of [2500, 1750 cm^{-1}]. But curiously the lowest energy optical transitions observed for (b) the singlet (green, solid) and triplet (blue, dash-dot-dot) negative polaron are shown to be in resonance with two peaks in (a) between [1750, 1450 cm^{-1}]. The peak (a) at 1450 cm^{-1} we attribute to N–H bending modes of the ethylammonium cations while the peak around 1600 cm^{-1} we attribute to C=O stretching modes of the acetate anions. From previous work⁴³ we have shown that for this specific surface chemistry only the acetate anions contribute electronic density to the surface of the NC (chemisorbed) while the ethylammonium cations are bound to the surface due to electrostatic attraction (physisorbed). This implies that the N–H vibrational modes do not contribute significantly to nonradiative recombination rates while the C=O stretching modes will. This is due to nonadiabatic coupling being proportional to the orbital overlap between Pb^{2+} or Br^- ions at the surface and the COO^- or NH_3^+ functional groups of the passivation ligands. We also note that the C=O mode is in resonance with the lowest energy optical transition for the negative triplet model and off-resonance of the negative singlet model. This is likely the source of the 2 orders of magnitude difference between their respective nonradiative recombination rates, as observed in [Table 2](#).

Within the mixed quantum-classical methodology used here, we note three features that have been neglected in this work that may have affected the computed values of radiative and nonradiative recombination rates for our model: (i) electronic

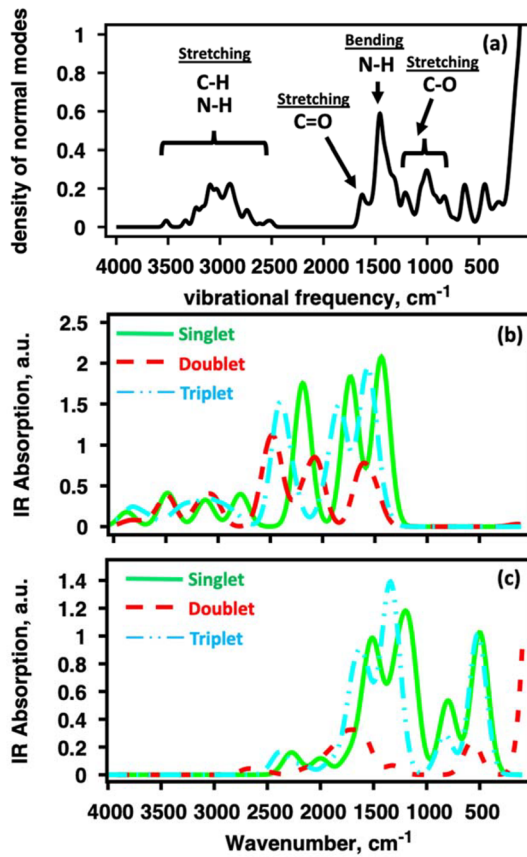


Figure 7. Comparing (a) the normal modes of vibration of a ligand terminated perovskite surface $\text{Cs}_8\text{Pb}_{12}\text{Br}_{32}$ to the IR absorption spectra of the (b) negative polaron models and (c) positive polaron models. It is observed that in the range $[2000, 2500] \text{ cm}^{-1}$ there is a mismatch between the vibrational modes provided by (a) the surface ligands and (b) energy of transitions between polaron states. For (c) the positive polaron it is seen that there are vibrational modes in resonance with transitions between polaronic states.

coherence associated with polaron formation; (ii) excited-state trajectory at lower temperature; and (iii) neglect of Bose–Einstein distributions for phonon occupations.

- (i) Within our density-matrix based excited-state dynamics calculations we implement the secular approximation,⁷⁶ meaning we assume instantaneous decay of the off-diagonal elements and only account for changes in occupations (diagonal elements of the Redfield tensor) which is legitimate on time scale $t > t_{\text{decoh}}$ and $t > t_{\text{dephas}}$. Typically electronic resonances decay (i.e., dephasing) within the 10^1 fs time scale and provide small corrections for nonradiative recombination rates, as observed when implemented into surface-hopping based excited-state dynamics.⁷⁷ Polarons are expected to increase electronic coherence times due to the screening of high energy longitudinal optical (LO) phonon modes. Accounting for electronic coherences would be expected to reduce the nonradiative recombination rates which would increase the computed PLQYs.
- (ii) For the excited-state trajectories explored here, we use a temperature of 300 K. By exploring a cooled thermal environment, such as 77 K (liquid N_2 temperatures), higher frequency phonon modes would not be active resulting in an extended nonradiative lifetime. With

reduced temperature it would also be expected that electronic coherences would also be extended which would decrease the nonradiative recombination rate.

- (iii) Within our mixed quantum-classical methodology we treat nuclear degrees of freedom as classical point particles which have a continuous energy spectrum. Since we neglect nuclear quantization we do not have discrete activation of certain vibrational modes for temperatures $kT \geq \hbar\omega_{\text{vib}}$. This implies that the contribution of higher energy vibrational modes in the model is overestimated, providing a faster nonradiative transition.

V. CONCLUSIONS

Lead-halide perovskites have been shown to be a promising material for next-generation light emitting devices due to tunable emission across the visible spectrum. They have also shown efficient application to photovoltaic devices in part due to the extended nonradiative lifetimes of photoinduced charges carriers, which has been attributed to large polaron formation producing simultaneous positive and negative polarons. Large polarons, quasiparticles which form in lead-halide perovskites due to their “soft” ionic lattice, are expected to show two contrasting absorption mechanisms: dipole-allowed transitions within the bound polaron potential well and photoionization of the bound polaron into the conduction/valence band. Photoexcitations within the polaron potential well produce an excited “hot-polaron” which can dissipate energy by using radiative or nonradiative relaxation mechanisms. We hypothesize that hot-polarons in perovskites have the ability to emit electromagnetic radiation in the IR range due to (i) inverse occupation within the potential well and (ii) bright electronic transitions within the polaron potential well. To test this, we implement mixed quantum-classical methodologies to model photophysical features of individual positive and negative polarons, with various spin multiplicities, in an atomistic CsPbBr_3 nanocrystal model fully passivated with organic ligands.

For the impact of polaron formation on the lead halide perovskite lattice, we found that positive and negative polarons show contrasting patterns for the $\text{Pb}-\text{Br}$ and $\text{Br}-\text{Br}$ ion pairs. Specifically, the positive polaron increases coordination number and decreases distances between $\text{Br}-\text{Br}$ atoms while the negative polaron increased coordination number and decreased bond distances between $\text{Pb}-\text{Br}$. This is rationalized in terms of oxidation (reduction) and reduced (increased) electronegativity due to positive (negative) polaron formation.

For spectral features, we implement two approaches: absorption spectra of individual polarons in the IOA and PL properties of individual polarons by implementing excited-state dynamics in the density matrix formalism which couple electronic and nuclear degrees of freedom. Interestingly, polaronic states involve frontier orbitals which exhibit certain spatial symmetry and patterns of electronic energy spacing compared to hydrogenic models. Thus, we analyze electronic transitions in terms of spatial symmetry $s_{h/e}$, $p_{h/e}$, and $d_{h/e}$ where h refers to positive polarons (holes) and e refers to negative polarons (electrons). It has been found that the spin multiplicity of the polaronic state drastically affects the observed optoelectronic properties. Specifically, the singlet and triplet multiplicities for both the positive and negative polaron models show bright lowest energy absorption

transitions and PL which we ascribe to $s_{h/e} \rightarrow p_{h/e}$ types of transitions. The doublet configuration shows 4×–5× reduced absorption intensities compared to the respective singlet or triplet multiplicity and vanishing PL due to its lowest energy transition being of $s_{h/e} \rightarrow s_{h/e}$ character.

The polaron models show low PLQY (10^{-4} – 10^{-8}) due to the large difference in time scales of radiative recombination (1–10 μ s) and nonradiative recombination (10 ns–1 ps). To explain the wide range of nonradiative recombination rates, we implement normal-mode analysis where vibrations are provided from the inorganic CsPbBr_3 lattice and from organic–inorganic interaction at the NC surface. For the system with the slowest nonradiative recombination rate (negative, singlet) we find there are a lack of *active* normal modes in resonance with the lowest energy transition from the polaron RES to the PGS. While in contrast, the models which displayed faster nonradiative recombination had active normal modes in resonance with their lowest energy optical transition. Specifically, the acetate anions contribute electronic density to the surface of the NC (chemisorbed) while the ethylammonium cations are bound to the surface due to electrostatic attraction (physisorbed). This implies that the N–H modes are *spectator* modes that do not contribute significantly to the nonradiative recombination rates while the C=O stretching modes are *active*.

There are at least two factors which affect nonradiative recombination and PLQY of a given polaron in our model: (i) a resonance condition between energy of electronic transition $\Delta E(\text{RES} \rightarrow \text{PGS})$ and frequency of phonon ω_{ph} accepting this quantum of energy $\Delta E \approx \hbar\omega_{ph}$ and (ii) spatial hybridization of the polaron with the surface passivation ligands which have phonons with normal-mode frequencies ω_{ph} . From our excited-state dynamics simulations we find that both the negative and positive polaron are emissive with the negative polaron showing orders of magnitude higher PLQY than the positive polaron. We attribute this to ligand vibrational modes from the surface which are in resonance with the positive polaron PL transitions, but off-resonance with the negative polaron PL transitions. The hypothesis of large polaron emission is partially supported by the atomistic simulations. Due to approximations in our methodology it is likely that the computed efficiency of polaron emission is underestimated, with an emphasis on the role of coherence/dephasing which would likely decrease the rate of nonradiative recombination. Inclusion of these effects into excited-state dynamics would give a clearer picture of the mechanisms of large polaron emission in APbX_3 perovskite materials. Implications of this work could be toward utilizing large polarons as mid-IR and far-IR emission sources.

ASSOCIATED CONTENT

Supporting Information

The Supporting Information is available free of charge at <https://pubs.acs.org/doi/10.1021/acs.jpcc.9b08044>.

Comments on validity of s, p, d notations; additional methodology used in this study: conversion of nonadiabatic coupling into state-to-state transitions, expectation values for excited-state observables, normal-mode analysis; illustration of the atomistic model used; diagram of polaron electronic structure and polaron formation in the atomistic model; energy fluctuations of SKSO orbitals along the MD trajectory; Redfield tensor

of additional models used in this work; elements of Redfield tensor which correspond to carrier cooling transitions and nonradiative recombination transitions; hot-carrier cooling dynamics for the doublet positive polaron model and triplet negative polaron; explicit changes in occupations along the excited-state trajectory for all models investigated; comparing the computed kinetics of hot-polaron carrier cooling to an exponential fit; comparing the hot-carrier cooling times of polaronic models to free-carrier models; radiative relaxation along the excited-state trajectory for the positive doublet and negative triplet polaron models; comparison of the polaron PL spectrum to their respective absorption spectrum to identify the characteristic emission transition; thin-film $\text{Cs}_8\text{Pb}_{12}\text{Br}_{32}$ passivated with 4 CH_3COO^- anions and 4 $\text{CH}_3\text{CH}_2\text{NH}_3^+$ cation ligands used for normal-mode analysis; table of polaron binding energies and square deviation of nuclear reorganization ([PDF](#))

AUTHOR INFORMATION

Corresponding Author

*E-mail: dmitri.kilin@ndsu.edu.

ORCID

Dmitri Kilin: [0000-0001-7847-5549](https://orcid.org/0000-0001-7847-5549)

Notes

The authors declare no competing financial interest.

ACKNOWLEDGMENTS

NSF CHE 1800476. The authors acknowledge the DOE BES NERSC facility for computational resources, allocation award #91202, “Computational Modeling of Photo-catalysis and Photo-induced Charge Transfer Dynamics on Surfaces” supported by the Office of Science of the DOE under contract no. DE-AC02-05CH11231. The authors would like to thank Douglas Jennewein for support and maintaining the High-Performance Computing system at the University of South Dakota. The work of T.M.I. is performed under the state assignment of IGM SB RAS, and T.M.I. gratefully acknowledges financial support of the Ministry of Education and Science of the Russian Federation in the framework of the Increase Competitiveness Program of NUST MISIS (No. K3-2018-022) implemented by a governmental decree dated 16th of March 2013, N 211. The calculations were partially performed at supercomputer cluster “Cherry” provided by the Materials Modeling and Development Laboratory at NUST “MISIS” (supported via the Grant from the Ministry of Education and Science of the Russian Federation No. 14.Y26.31.0005).

REFERENCES

- (1) Englman, R.; Jortner, J. Energy Gap Law for Radiationless Transitions in Large Molecules. *Mol. Phys.* **1970**, *18* (2), 145–164.
- (2) Lu, H.; Carroll, G. M.; Neale, N. R.; Beard, M. C. Infrared Quantum Dots: Progress, Challenges, and Opportunities. *ACS Nano* **2019**, *13* (2), 939–953.
- (3) Steenbergen, E. H.; Connelly, B. C.; Metcalfe, G. D.; Shen, H.; Wraback, M.; Lubyshev, D.; Qiu, Y.; Fastenau, J. M.; Liu, A. W. K.; Elhamri, S.; Cellek, O. O.; Zhang, Y. H. Significantly Improved Minority Carrier Lifetime Observed in a Long-Wavelength Infrared III-V Type-II Superlattice Comprised of InAs/InAsSb. *Appl. Phys. Lett.* **2011**, *99* (25), 251110.

(4) Lei, W.; Antoszewski, J.; Faraone, L. Progress, Challenges, and Opportunities for HgCdTe Infrared Materials and Detectors. *Appl. Phys. Rev.* **2015**, *2* (4), 041303.

(5) Saha, A.; Gifford, B. J.; He, X.; Ao, G.; Zheng, M.; Kataura, H.; Htoon, H.; Kilina, S.; Tretiak, S.; Doorn, S. K. Narrow-Band Single-Photon Emission through Selective Aryl Functionalization of Zigzag Carbon Nanotubes. *Nat. Chem.* **2018**, *10* (11), 1089–1095.

(6) Katan, C.; Mercier, N.; Even, J. Quantum and Dielectric Confinement Effects in Lower-Dimensional Hybrid Perovskite Semiconductors. *Chem. Rev.* **2019**, *119* (5), 3140–3192.

(7) Keldysh, L. V. Coulomb Interaction in Thin Semiconductor and Semimetal Films. *JETP Lett.* **1979**, *29* (11), 658.

(8) Chen, G.; Tien, C. L. Thermal Conductivities of Quantum Well Structures. *J. Thermophys. Heat Transfer* **1993**, *7* (2), 311–318.

(9) Song, J.; Li, J.; Li, X.; Xu, L.; Dong, Y.; Zeng, H. Quantum Dot Light-Emitting Diodes Based on Inorganic Perovskite Cesium Lead Halides (CsPbX_3). *Adv. Mater.* **2015**, *27* (44), 7162–7167.

(10) Xing, G.; Wu, B.; Wu, X.; Li, M.; Du, B.; Wei, Q.; Guo, J.; Yeow, E. K. L.; Sum, T. C.; Huang, W. Transcending the Slow Bimolecular Recombination in Lead-Halide Perovskites for Electroluminescence. *Nat. Commun.* **2017**, *8* (1), 14558.

(11) Yuan, M.; Quan, L. N.; Comin, R.; Walters, G.; Sabatini, R.; Voznyy, O.; Hoogland, S.; Zhao, Y.; Beauregard, E. M.; Kanjanaboos, P.; Lu, Z.; Kim, D. H.; Sargent, E. H. Perovskite Energy Funnels for Efficient Light-Emitting Diodes. *Nat. Nanotechnol.* **2016**, *11*, 872.

(12) Lin, K.; Xing, J.; Quan, L. N.; de Arquer, F. P. G.; Gong, X.; Lu, J.; Xie, L.; Zhao, W.; Zhang, D.; Yan, C.; Li, W.; Liu, X.; Lu, Y.; Kirman, J.; Sargent, E. H.; Xiong, Q.; Wei, Z. Perovskite Light-Emitting Diodes with External Quantum Efficiency Exceeding 20 Per Cent. *Nature* **2018**, *562* (7726), 245–248.

(13) Kim, Y.-H.; Wolf, C.; Kim, Y.-T.; Cho, H.; Kwon, W.; Do, S.; Sadhanala, A.; Park, C. G.; Rhee, S.-W.; Im, S. H.; Friend, R. H.; Lee, T.-W. Highly Efficient Light-Emitting Diodes of Colloidal Metal–Halide Perovskite Nanocrystals Beyond Quantum Size. *ACS Nano* **2017**, *11* (7), 6586–6593.

(14) Yan, F.; Xing, J.; Xing, G.; Quan, L.; Tan, S. T.; Zhao, J.; Su, R.; Zhang, L.; Chen, S.; Zhao, Y.; Huan, A.; Sargent, E. H.; Xiong, Q.; Demir, H. V. Highly Efficient Visible Colloidal Lead–Halide Perovskite Nanocrystal Light-Emitting Diodes. *Nano Lett.* **2018**, *18* (5), 3157–3164.

(15) Nie, W.; Tsai, H.; Asadpour, R.; Blancon, J.-C.; Neukirch, A. J.; Gupta, G.; Crochet, J. J.; Chhowalla, M.; Tretiak, S.; Alam, M. A.; Wang, H.-L.; Mohite, A. D. High-Efficiency Solution-Processed Perovskite Solar Cells with Millimeter-Scale Grains. *Science* **2015**, *347* (6221), 522.

(16) Tsai, H.; Nie, W.; Blancon, J. C.; Stoumpos, C. C.; Asadpour, R.; Harutyunyan, B.; Neukirch, A. J.; Verduzco, R.; Crochet, J. J.; Tretiak, S.; Pedesseau, L.; Even, J.; Alam, M. A.; Gupta, G.; Lou, J.; Ajayan, P. M.; Bedzyk, M. J.; Kanatzidis, M. G.; Mohite, A. D. High-Efficiency Two-Dimensional Ruddlesden–Popper Perovskite Solar Cells. *Nature* **2016**, *536* (7616), 312–6.

(17) Luo, Q.; Ma, H.; Hou, Q.; Li, Y.; Ren, J.; Dai, X.; Yao, Z.; Zhou, Y.; Xiang, L.; Du, H.; He, H.; Wang, N.; Jiang, K.; Lin, H.; Zhang, H.; Guo, Z. All-Carbon-Electrode-Based Endurable Flexible Perovskite Solar Cells. *Adv. Funct. Mater.* **2018**, *28* (11), 1706777.

(18) Sanehira, E. M.; Marshall, A. R.; Christians, J. A.; Harvey, S. P.; Ciesielski, P. N.; Wheeler, L. M.; Schulz, P.; Lin, L. Y.; Beard, M. C.; Luther, J. M. Enhanced Mobility CsPbI_3 Quantum Dot Arrays for Record-Efficiency, High-Voltage Photovoltaic Cells. *Sci. Adv.* **2017**, *3* (10), eaao4204.

(19) Luo, Q.; Ma, H.; Hao, F.; Hou, Q.; Ren, J.; Wu, L.; Yao, Z.; Zhou, Y.; Wang, N.; Jiang, K.; Lin, H.; Guo, Z. Carbon Nanotube Based Inverted Flexible Perovskite Solar Cells with All-Inorganic Charge Contacts. *Adv. Funct. Mater.* **2017**, *27* (42), 1703068.

(20) Luo, Q.; Chen, H.; Lin, Y.; Du, H.; Hou, Q.; Hao, F.; Wang, N.; Guo, Z.; Huang, J. Discrete Iron(III) Oxide Nanoislands for Efficient and Photostable Perovskite Solar Cells. *Adv. Funct. Mater.* **2017**, *27* (34), 1702090.

(21) Ren, J.; Luo, Q.; Hou, Q.; Chen, H.; Liu, T.; He, H.; Wang, J.; Shao, Q.; Dong, M.; Wu, S.; Wang, N.; Lin, J.; Guo, Z. Suppressing Charge Recombination and Ultraviolet Light Degradation of Perovskite Solar Cells Using Silicon Oxide Passivation. *ChemElectroChem* **2019**, *6* (12), 3167–3174.

(22) Cao, B.; Liu, H.; Yang, L.; Li, X.; Liu, H.; Dong, P.; Mai, X.; Hou, C.; Wang, N.; Zhang, J.; Fan, J.; Gao, Q.; Guo, Z. Interfacial Engineering for High-Efficiency Nanorod Array-Structured Perovskite Solar Cells. *ACS Appl. Mater. Interfaces* **2019**, *11* (37), 33770–33780.

(23) Hou, Q.; Ren, J.; Chen, H.; Yang, P.; Shao, Q.; Zhao, M.; Zhao, X.; He, H.; Wang, N.; Luo, Q.; Guo, Z. Synergistic Hematite–Fullerene Electron-Extracting Layers for Improved Efficiency and Stability in Perovskite Solar Cells. *ChemElectroChem* **2018**, *5* (5), 726–731.

(24) Yang, L.; Wang, X.; Mai, X.; Wang, T.; Wang, C.; Li, X.; Murugadoss, V.; Shao, Q.; Angaiah, S.; Guo, Z. Constructing Efficient Mixed-Ion Perovskite Solar Cells Based on TiO_2 Nanorod Array. *J. Colloid Interface Sci.* **2019**, *534*, 459–468.

(25) Guo, Y.; Xue, Y.; Li, X.; Li, C.; Song, H.; Niu, Y.; Liu, H.; Mai, X.; Zhang, J.; Guo, Z., Effects of Transition Metal Substituents on Interfacial and Electronic Structure of $\text{CH}_3\text{NH}_3\text{PbI}_3/\text{TiO}_2$ Interface: A First-Principles Comparative Study. *Nanomaterials* **2019**, *9* (7), 966.

(26) Yost, A. J.; Pimachev, A.; Ho, C.-C.; Darling, S. B.; Wang, L.; Su, W.-F.; Dahnovsky, Y.; Chien, T. Coexistence of Two Electronic Nano-Phases on a $\text{CH}_3\text{NH}_3\text{PbI}_{3-x}\text{Cl}_x$ Surface Observed in STM Measurements. *ACS Appl. Mater. Interfaces* **2016**, *8* (42), 29110–29116.

(27) Protesescu, L.; Yakunin, S.; Bodnarchuk, M. I.; Krieg, F.; Caputo, R.; Hendon, C. H.; Yang, R. X.; Walsh, A.; Kovalenko, M. V. Nanocrystals of Cesium Lead Halide Perovskites (CsPbX_3 , X = Cl, Br, and I): Novel Optoelectronic Materials Showing Bright Emission with Wide Color Gamut. *Nano Lett.* **2015**, *15* (6), 3692–6.

(28) Zhang, D.; Eaton, S. W.; Yu, Y.; Dou, L.; Yang, P. Solution-Phase Synthesis of Cesium Lead Halide Perovskite Nanowires. *J. Am. Chem. Soc.* **2015**, *137* (29), 9230–9233.

(29) Stranks, S. D.; Snaith, H. J. Metal–Halide Perovskites for Photovoltaic and Light-Emitting Devices. *Nat. Nanotechnol.* **2015**, *10*, 391.

(30) Tsai, H.; Nie, W.; Blancon, J.-C.; Stoumpos, C. C.; Asadpour, R.; Harutyunyan, B.; Neukirch, A. J.; Verduzco, R.; Crochet, J. J.; Tretiak, S.; Pedesseau, L.; Even, J.; Alam, M. A.; Gupta, G.; Lou, J.; Ajayan, P. M.; Bedzyk, M. J.; Kanatzidis, M. G.; Mohite, A. D. High-Efficiency Two-Dimensional Ruddlesden–Popper Perovskite Solar Cells. *Nature* **2016**, *536*, 312.

(31) Becker, M. A.; Vaxenburg, R.; Nedelcu, G.; Sercel, P. C.; Shabaev, A.; Mehl, M. J.; Michopoulos, J. G.; Lambrakos, S. G.; Bernstein, N.; Lyons, J. L.; Stöferle, T.; Mahrt, R. F.; Kovalenko, M. V.; Norris, D. J.; Raino, G.; Efros, A. L. Bright Triplet Excitons in Caesium Lead Halide Perovskites. *Nature* **2018**, *553*, 189.

(32) Zhu, X. Y.; Podzorov, V. Charge Carriers in Hybrid Organic–Inorganic Lead Halide Perovskites Might Be Protected as Large Polarons. *J. Phys. Chem. Lett.* **2015**, *6* (23), 4758–4761.

(33) Park, M.; Neukirch, A. J.; Reyes-Lillo, S. E.; Lai, M.; Ellis, S. R.; Dietze, D.; Neaton, J. B.; Yang, P.; Tretiak, S.; Mathies, R. A. Excited-State Vibrational Dynamics toward the Polaron in Methylammonium Lead Iodide Perovskite. *Nat. Commun.* **2018**, *9* (1), 2525.

(34) Neukirch, A. J.; Nie, W.; Blancon, J.-C.; Appavoo, K.; Tsai, H.; Sfeir, M. Y.; Katan, C.; Pedesseau, L.; Even, J.; Crochet, J. J.; Gupta, G.; Mohite, A. D.; Tretiak, S. Polaron Stabilization by Cooperative Lattice Distortion and Cation Rotations in Hybrid Perovskite Materials. *Nano Lett.* **2016**, *16* (6), 3809–3816.

(35) Miyata, K.; Meggiolaro, D.; Trinh, M. T.; Joshi, P. P.; Mosconi, E.; Jones, S. C.; De Angelis, F.; Zhu, X. Y.; Large Polarons in Lead Halide Perovskites. *Sci. Adv.* **2017**, *3* (8), e1701217

(36) Devreese, J. T.; Alexandrov, A. S. Fröhlich Polaron and Bipolaron: Recent Developments. *Rep. Prog. Phys.* **2009**, *72* (6), 066501.

(37) Kartheuser, E.; Evrard, R.; Devreese, J. Mechanism of Absorption of Light by Free Continuum Polarons. *Phys. Rev. Lett.* **1969**, *22* (3), 94–97.

(38) Emin, D. Optical Properties of Large and Small Polarons and Bipolarons. *Phys. Rev. B: Condens. Matter Mater. Phys.* **1993**, *48* (18), 13691–13702.

(39) Munson, K. T.; Kennehan, E. R.; Doucette, G. S.; Asbury, J. B. Dynamic Disorder Dominates Delocalization, Transport, and Recombination in Halide Perovskites. *Chem.* **2018**, *4* (12), 2826–2843.

(40) Munson, K. T.; Doucette, G. S.; Kennehan, E. R.; Swartzfager, J. R.; Asbury, J. B. Vibrational Probe of the Structural Origins of Slow Recombination in Halide Perovskites. *J. Phys. Chem. C* **2019**, *123* (12), 7061–7073.

(41) Emin, D. Barrier to Recombination of Oppositely Charged Large Polarons. *J. Appl. Phys.* **2018**, *123* (5), 055105.

(42) Zhang, M.; Zhang, X.; Lin, H.-Q.; Lu, G. Radiative Recombination of Large Polarons in Halide Perovskites. *J. Phys.: Condens. Matter* **2019**, *31* (16), 165701.

(43) Forde, A.; Inerbaev, T.; Hobbie, E. K.; Kilin, D. S. Excited-State Dynamics of a CsPbBr_3 Nanocrystal Terminated with Binary Ligands: Sparse Density of States with Giant Spin–Orbit Coupling Suppresses Carrier Cooling. *J. Am. Chem. Soc.* **2019**, *141* (10), 4388–4397.

(44) Vogel, D. J.; Kryjevski, A.; Inerbaev, T. M.; Kilin, D. S. Photoinduced Single- and Multiple- Electron Dynamics Processes Enhanced by Quantum Confinement in Lead Halide Perovskite Quantum Dots. *J. Phys. Chem. Lett.* **2017**, *8* (13), 3032–3039.

(45) Inerbaev, T. M.; Hoefelmeyer, J. D.; Kilin, D. S. Photoinduced Charge Transfer from Titania to Surface Doping Site. *J. Phys. Chem. C* **2013**, *117* (19), 9673–9692.

(46) Kryjevski, A.; Mihaylov, D.; Kilina, S.; Kilin, D. Multiple Exciton Generation in Chiral Carbon Nanotubes: Density Functional Theory Based Computation. *J. Chem. Phys.* **2017**, *147* (15), 154106.

(47) Hammes-Schiffer, S.; Tully, J. C. Proton Transfer in Solution – Molecular Dynamics with Quantum Transitions. *J. Chem. Phys.* **1994**, *101* (6), 4657–4667.

(48) Vogel, D. J.; Kilin, D. S. First Principles Treatment of Photoluminescence in Semiconductors. *J. Phys. Chem. C* **2015**, *119* (50), 27954–27964.

(49) Han, Y.; Meng, Q.; Rasulev, B.; May, P. S.; Berry, M. T.; Kilin, D. S. Photoinduced Charge Transfer Versus Fragmentation Pathways in Lanthanum Cyclopentadienyl Complexes. *J. Chem. Theory Comput.* **2017**, *13* (9), 4281–4296.

(50) Kilina, S.; Kilin, D.; Tretiak, S. Light-Driven and Phonon-Assisted Dynamics in Organic and Semiconductor Nanostructures. *Chem. Rev.* **2015**, *115* (12), 5929–5978.

(51) Juarez-Perez, E. J.; Sanchez, R. S.; Badia, L.; Garcia-Belmonte, G.; Kang, Y. S.; Mora-Sero, I.; Bisquert, J. Photoinduced Giant Dielectric Constant in Lead Halide Perovskite Solar Cells. *J. Phys. Chem. Lett.* **2014**, *5* (13), 2390–2394.

(52) Barth, U. v.; Hedin, L. A Local Exchange-Correlation Potential for the Spin Polarized Case. I. *J. Phys. C: Solid State Phys.* **1972**, *5* (13), 1629–1642.

(53) Kubler, J.; Hock, K. H.; Sticht, J.; Williams, A. R. Density Functional Theory of Non-Collinear Magnetism. *J. Phys. F: Met. Phys.* **1988**, *18* (3), 469–483.

(54) Redfield, A. G. On the Theory of Relaxation Processes. *IBM J. Res. Dev.* **1957**, *1* (1), 19–31.

(55) Jean, J. M.; Friesner, R. A.; Fleming, G. R. Application of a Multilevel Redfield Theory to Electron Transfer in Condensed Phases. *J. Chem. Phys.* **1992**, *96* (8), 5827–5842.

(56) Einstein, A. On the Quantum Theory of Radiation. *Physikalische Zeitschrift* **1917**, *18*, 121.

(57) Forde, A.; Inerbaev, T.; Kilin, D. Role of Cation-Anion Organic Ligands for Optical Properties of Fully Inorganic Perovskite Quantum Dots. *MRS Advances* **2018**, *3* (55), 3255–3261.

(58) Perdew, J. P.; Burke, K.; Ernzerhof, M. Generalized Gradient Approximation Made Simple. *Phys. Rev. Lett.* **1997**, *78* (7), 1396–1396.

(59) Blöchl, P. E. Projector Augmented-Wave Method. *Phys. Rev. B: Condens. Matter Mater. Phys.* **1994**, *50* (24), 17953–17979.

(60) Kresse, G.; Joubert, D. From Ultrasoft Pseudopotentials to the Projector Augmented-Wave Method. *Phys. Rev. B: Condens. Matter Mater. Phys.* **1999**, *59* (3), 1758–1775.

(61) Kresse, G.; Furthmüller, J. Efficiency of Ab-Initio Total Energy Calculations for Metals and Semiconductors Using a Plane-Wave Basis Set. *Comput. Mater. Sci.* **1996**, *6* (1), 15–50.

(62) Neugebauer, J.; Scheffler, M. Adsorbate-Substrate and Adsorbate-Adsorbate Interactions of Na and K Adlayers on $\text{Al}(111)$. *Phys. Rev. B: Condens. Matter Mater. Phys.* **1992**, *46* (24), 16067–16080.

(63) Makov, G.; Payne, M. C. Periodic Boundary Conditions in Ab Initio Calculations. *Phys. Rev. B: Condens. Matter Mater. Phys.* **1995**, *51* (7), 4014–4022.

(64) Brown, S. L.; Vogel, D. J.; Miller, J. B.; Inerbaev, T. M.; Anthony, R. J.; Kortshagen, U. R.; Kilin, D. S.; Hobbie, E. K. Enhancing Silicon Nanocrystal Photoluminescence through Temperature and Microstructure. *J. Phys. Chem. C* **2016**, *120* (33), 18909–18916.

(65) Makarov, N. S.; Guo, S.; Isaenko, O.; Liu, W.; Robel, I.; Klimov, V. I. Spectral and Dynamical Properties of Single Excitons, Biexcitons, and Triions in Cesium-Lead-Halide Perovskite Quantum Dots. *Nano Lett.* **2016**, *16* (4), 2349–62.

(66) Yao, G.; Berry, M.; May, P. S.; Wang, J.; Kilin, D. S. Relationship between Site Symmetry, Spin State, and Doping Concentration for $\text{Co}(\text{Ii})$ or $\text{Co}(\text{Iii})$ in $\text{B}-\text{Nayf}_4$. *J. Phys. Chem. C* **2016**, *120* (14), 7785–7794.

(67) Neukirch, A. J.; Abate, I. I.; Zhou, L.; Nie, W.; Tsai, H.; Pedesseau, L.; Even, J.; Crochet, J. J.; Mohite, A. D.; Katan, C.; Tretiak, S. Geometry Distortion and Small Polaron Binding Energy Changes with Ionic Substitution in Halide Perovskites. *J. Phys. Chem. Lett.* **2018**, *9* (24), 7130–7136.

(68) Evans, T. J. S.; Miyata, K.; Joshi, P. P.; Maehrlein, S.; Liu, F.; Zhu, X. Y. Competition between Hot-Electron Cooling and Large Polaron Screening in CsPbBr_3 Perovskite Single Crystals. *J. Phys. Chem. C* **2018**, *122* (25), 13724–13730.

(69) He, J.; Vasenko, A. S.; Long, R.; Prezhdo, O. V. Halide Composition Controls Electron–Hole Recombination in Cesium–Lead Halide Perovskite Quantum Dots: A Time Domain Ab Initio Study. *J. Phys. Chem. Lett.* **2018**, *9* (8), 1872–1879.

(70) Hopper, T. R.; Gorodetsky, A.; Frost, J. M.; Müller, C.; Lovrincic, R.; Bakulin, A. A. Ultrafast Intraband Spectroscopy of Hot-Carrier Cooling in Lead-Halide Perovskites. *ACS Energy Lett.* **2018**, *3* (9), 2199–2205.

(71) Frost, J. M.; Whalley, L. D.; Walsh, A. Slow Cooling of Hot Polarons in Halide Perovskite Solar Cells. *ACS Energy Lett.* **2017**, *2* (12), 2647–2652.

(72) Li, M.; Bhaumik, S.; Goh, T. W.; Kumar, M. S.; Yantara, N.; Grätzel, M.; Mhaisalkar, S.; Mathews, N.; Sum, T. C. Slow Cooling and Highly Efficient Extraction of Hot Carriers in Colloidal Perovskite Nanocrystals. *Nat. Commun.* **2017**, *8*, 14350.

(73) Papagiorgis, P.; Protesescu, L.; Kovalenko, M. V.; Othonos, A.; Itskos, G. Long-Lived Hot Carriers in Formamidinium Lead Iodide Nanocrystals. *J. Phys. Chem. C* **2017**, *121* (22), 12434–12440.

(74) Butkus, J.; Vashishtha, P.; Chen, K.; Gallaher, J. K.; Prasad, S. K. K.; Metin, D. Z.; Laufersky, G.; Gaston, N.; Halpert, J. E.; Hodgkiss, J. M. The Evolution of Quantum Confinement in CsPbBr_3 Perovskite Nanocrystals. *Chem. Mater.* **2017**, *29* (8), 3644–3652.

(75) Li, W.; Zhou, L.; Prezhdo, O. V.; Akimov, A. V. Spin–Orbit Interactions Greatly Accelerate Nonradiative Dynamics in Lead Halide Perovskites. *ACS Energy Lett.* **2018**, *3* (9), 2159–2166.

(76) May, V.; Kuhn, O. *Charge and Energy Transfer Dynamics in Molecular Systems*. Wiley-VCH: 2004.

(77) Jaeger, H. M.; Fischer, S.; Prezhdo, O. V. Decoherence-Induced Surface Hopping. *J. Chem. Phys.* **2012**, *137* (22), 22A545